J Sci Comput
DOI 10.1007/s10915-014-9864-7

Dispersion Relation Preserving Combined Compact Difference Schemes for Flow Problems

C. H. Yu · Yogesh G. Bhumkar · Tony W. H. Sheu

Received: 21 September 2013 / Revised: 26 February 2014 / Accepted: 28 April 2014
© Springer Science+Business Media New York 2014

Abstract In this work, we have proposed two new combined compact difference (CCD) schemes for the solution of Navier–Stokes equations. These spatial discretization schemes have not only high spectral resolution for obtaining first and second derivative terms, but also have improved dispersion relation preserving properties when the fourth-order four-stage Runge–Kutta scheme is used for time integration. Out of the two proposed CCD schemes, the first scheme has upwind stencil, while the second scheme has a central stencil. Important numerical properties of these schemes have been analyzed and their effectiveness have been shown by solving the model wave equations, as well as Navier–Stokes equations. Results show that the upwind CCD scheme is suitable for high accuracy large eddy simulation of transitional and turbulent flowfields.

Keywords Combined compact difference schemes · Dispersion relation preserving schemes · Lid driven cavity · q-waves · Aliasing error

C. H. Yu
Department of Engineering Science and Ocean Engineering, National Taiwan University, No. 1, Sec. 4, Roosevelt Road, Taipei, Taiwan, ROC

C. H. Yu
Department of Ocean Science and Engineering, Zhejiang University, Yuhangtang Road, Hangzhou , Zhejiang, People's Republic of China

Y. G. Bhumkar · T. W. H. Sheu (✉)
Center of Advanced Study in Theoretical Sciences, National Taiwan University, No. 1, Sec. 4, Roosevelt Road, Taipei, Taiwan, ROC
e-mail: twhsheu@ntu.edu.tw

Y. G. Bhumkar
School of Mechanical Sciences, Indian Institute of Technology Bhubaneswar, Bhubaneswar, Odisha, India
e-mail: bhumkar@iitbbs.ac.in

Published online: 11 May 2014

1 Introduction

A space-time accurate numerical simulation of fluid flow and heat transfer problems requires higher spatial resolution and dispersion relation preservation (DRP) properties [1–3,13]. Such schemes act as an important numerical tool to solve complex physical problems displaying a large bandwidth of spatio-temporal scales. Although a very fine mesh correctly captures the important spatial flow structures, use of higher resolution methods offers similar spectral accuracy with fewer grid points. This benefits in saving considerable computational cost. Compact schemes have been studied intensively in this regard [4–12,14–17].

For approximating spatial derivatives, any numerical scheme can be represented in the matrix form as $[A]\{u'\} = [B]\{u\}$ or $\{u'\} = [D]\{u\}$, where $[D] = [A]^{-1}[B]$. Matrix $[A]$ for an explicit scheme is an identity matrix in contrast to tri-diagonal or penta-diagonal matrix for compact schemes. This results in a sparse matrix $[D]$ for explicit schemes, in comparison to large band-width matrix $[D]$ for compact schemes. Thus, while evaluating spatial derivatives using compact schemes, many nodes in the domain contribute to achieve higher spectral resolution [19]. This idea is further used to develop a three point combined compact difference scheme (CCD) in [20] in which first and second derivative terms are implicitly evaluated simultaneously. Combined calculation of the first and the second derivatives makes the scheme more compact and accurate than the compact difference schemes for first derivative. New boundary closure was suggested in [21] for obtaining better numerical properties and the corresponding dissipation and de-aliasing properties were discussed in [22]. Improvement in spectral properties of CCD schemes were further attempted in [9,17].

While developing new numerical schemes, one aims to achieve higher spectral resolution along with the ability to numerically preserve dispersion relation accurately over a considerable wavenumber range. This ensures each and every resolved component of energy to propagate at the correct physical speed. Fluid flow can exhibit complex phenomena which involve interactions among different scales. With this idea, a new DRP upwind CCD scheme has been developed in [1]. The proposed scheme in [1] has higher spectral resolution and better DRP properties as compared to the scheme proposed in [20].

However, compact schemes with high spectral resolution are also prone to aliasing error. While performing computations in the transformed plane both the linear, as well as, non-linear terms in the transformed governing equations contribute to aliasing error as these terms involve product of spatial derivative terms [19,22]. Researchers have proposed various ways to reduce aliasing error. Different formulation of the governing equations was suggested in [23,24] to control aliasing error. Discussion on aliasing error while performing computations on non-uniform grids was given in [11,25]. Use of multidimensional filter was recommended in [19,26] while the necessity of upwind CCD scheme was highlighted in [11,22] to take care of aliasing error. Thus while designing high accuracy DRP schemes, one should pay close attention to control aliasing error [19].

In the present work, we have extended this idea of developing new optimized CCD scheme and proposed two new central and an upwinded CCD schemes. Developed schemes have higher spectral resolution and improved DRP properties than the earlier proposed central scheme in [20] and upwinded scheme in [1]. We also discuss de-aliasing nature of the proposed upwind compact scheme here.

Numerical properties of the proposed schemes are analyzed using a global spectral analysis tool as in [5,6]. This full domain analysis explains simultaneous effects of one-sided boundary and near-boundary nodes on the important numerical properties everywhere in the domain. While analyzing high accuracy, explicit and implicit methods in [5], differences between

numerical properties of near boundary and central nodes are clearly indicated using this global matrix analysis methodology.

The full domain analysis approach [5,6] is completely different as compared to the popular semi-discretization eigen-value analysis approach attempted in many previous works. Unlike semi-discretization analysis approach, full domain analysis does not wrongly assume the time discretization as perfect entity. When one deals with analysis of unsteady flows, numerical properties must be obtained by considering space-time discretization together as in full domain analysis. The stable or unstable behavior of the numerical schemes depends significantly on the chosen time discretization scheme. Any attempt to draw conclusion about stability properties of the numerical scheme by considering just spatial derivative scheme is going to give a wrong picture and should not be attempted. In this regard, we have analyzed our proposed numerical schemes following full domain analysis of [6].

In [1,3], DRP schemes were constructed by optimizing the spectral resolution of the spatial derivative terms. In contrast, authors in [13] proposed new DRP schemes by combined optimization of spatial and temporal discretization schemes. Since the dispersion relation involves the relation between the spatial and temporal scales, combined optimization of spatial and temporal discretization schemes was emphasized in [13]. For the proposed schemes, we have obtained numerical group velocity contours for the solution of one dimensional wave equation following [5,6] to mark improvements in DRP properties.

Proposed upwind and central CCD schemes have been identified as schemes A and B, respectively. The stencils and numerical properties for these schemes are discussed in the next section while the methodology to design the stencil for upwind CCD scheme has been given in the "Appendix" following the work of [1].

2 Numerical Properties for Non-periodic Problems Using Fourier–Laplace Spectral Theory

To analyze nodal properties for non-periodic problems, a matrix spectral analysis technique has been developed in [5,6,19]. In this work, we have used this methodology to obtain the numerical properties for the developed high spectral resolution DRP schemes. For any numerical scheme, the first derivative $f' = \frac{\partial f}{\partial x}$ can also be explicitly written as,

$$\{f'\} = \frac{1}{h}[C]\{f\} \tag{1}$$

where $\{f\}$ and $[C]$ are column vector and matrix, respectively, with h as the constant grid spacing.

Representation of numerically obtained first derivative at a grid point x_j in the spectral plane is given as $f'(x_j, t) = \int_{k_{min}}^{k_{max}} ik_{eq}\ F(k,t)\ e^{ikx_j}\ dk$. In this expression, k_{max} and k_{min} give the maximum and minimum resolved wavenumbers by the grid. Assuming the domain is divided into $N+1$ equi-spaced points with h as grid spacing, an expression for the equivalent wavenumber is given as [5,19,39],

$$ik_{eq}(x_j) = \frac{1}{h}\sum_{l=1}^{N+1} C_{lj} e^{ik(x_l - x_j)} \tag{2}$$

The term k_{eq} is in general a complex quantity, with its real part signifies the phase and the imaginary part represents the added numerical diffusion or anti-diffusion. We have analyzed

these properties for the CCD scheme with central stencil [20,39], upwind CCD scheme [1] and two new CCD schemes proposed in this work.

The CCD scheme in [20,39] is given as,

$$\frac{7}{16}\left(f'_{i+1}+f'_{i-1}\right)+f'_i-\frac{h}{16}\left(f''_{i+1}-f''_{i-1}\right)=\frac{15}{16h}\left(f_{i+1}-f_{i-1}\right) \tag{3}$$

$$\frac{9}{8h}\left(f'_{i+1}-f'_{i-1}\right)-\frac{1}{8}\left(f''_{i+1}+f''_{i-1}\right)+f''_i=\frac{3}{h^2}\left(f_{i+1}-2f_i+f_{i-1}\right) \tag{4}$$

For a non-periodic problem one needs four additional boundary stencils at the nodes 1 and $N+1$. These have been provided in [20] as,

$$f'_1+2f'_2-hf''_2=\frac{1}{h}\left(-3.5f_1+4f_2-0.5f_3\right), \tag{5}$$

$$hf''_1+5hf''_2-6f'_2=\frac{1}{h}\left(9f_1-12f_2+3f_3\right), \tag{6}$$

$$f'_{N+1}+2f'_N-hf''_N=\frac{-1}{h}\left(-3.5f_{N+1}+4f_N-0.5f_{N-1}\right), \tag{7}$$

$$hf''_{N+1}+5hf''_N+6f'_N=\frac{1}{h}\left(9f_{N+1}-12f_N+3f_{N-1}\right). \tag{8}$$

In [21], authors have proposed a modified CCD scheme ($NCCD$) with different near-boundary stencils as the above boundary closure leads to anti-diffusion. To determine first and second derivatives at $N+1$ grid points in the domain, one needs $2N+2$ equations. As explained in [21], Eq. (3) has been used for the nodes 3 to $N-1$ while Eq. (4) has been used for the nodes 2 to N. At the boundary points, explicit stencils for the first and second derivatives are provided at $j=1$: $f'_1=(-1.5f_1+2f_2-0.5f_3)/h$ and $f''_1=(f_1-2f_2+f_3)/h^2$ [21]. Derivatives at the point $N+1$ are obtained using the same stencils with a reverse sign on the right hand side. Four additional near-boundary stencils for the nodes 2 and N are provided to improve numerical diffusion at the near boundary points. These are given as,

$$\begin{aligned} f'_2=\frac{1}{h}\Bigg[&\left(\frac{2\beta_2}{3}-\frac{1}{3}\right)f_1-\left(\frac{8\beta_2}{3}+\frac{1}{2}\right)f_2+\left(4\beta_2+1\right)f_3.\\ &-\left(\frac{8\beta_2}{3}+\frac{1}{6}\right)f_4+\frac{2\beta_2}{3}f_5\Bigg], \end{aligned} \tag{9}$$

$$\begin{aligned} f'_N=\frac{-1}{h}\Bigg[&\left(\frac{2\beta_N}{3}-\frac{1}{3}\right)f_{N+1}-\left(\frac{8\beta_N}{3}+\frac{1}{2}\right)f_N+\left(4\beta_N+1\right)f_{N-1}\\ &-\left(\frac{8\beta_N}{3}+\frac{1}{6}\right)f_{N-2}+\frac{2\beta_N}{3}f_{N-3}\Bigg], \end{aligned} \tag{10}$$

$$f''_2=(f_1-2f_2+f_3)/h^2, \tag{11}$$

$$f''_N=(f_{N+1}-2f_N+f_{N-1})/h^2 \tag{12}$$

where $\beta_2=-0.025$ and $\beta_N=0.09$

In the present work, we have proposed and analyzed two new CCD schemes, schemes A and B. Stencil for scheme A is given as,

$$\begin{aligned} &a_{1u}f'_{i-1}+f'_i+a_{3u}f'_{i+1}+h\left(b_{1u}f''_{i-1}+b_{2u}f''_i+b_{3u}f''_{i+1}\right)\\ &\quad=\frac{1}{h}\left(c_{1u}f_{i-2}+c_{2u}f_{i-1}+c_{3u}f_i\right) \end{aligned} \tag{13}$$

$$\frac{9}{8h}\left(f'_{i+1}-f'_{i-1}\right)-\frac{1}{8}\left(f''_{i+1}+f''_{i-1}\right)+f''_i=\frac{3}{h^2}\left(f_{i+1}-2f_i+f_{i-1}\right) \tag{14}$$

The optimized coefficients in Eq. (13) are given as,

$$\begin{aligned} a_{1u} &= 0.888251792581;\ a_{3u} = 0.049229651564 \\ b_{1u} &= 0.150072398996;\ b_{2u} = -0.250712794122 \\ b_{3u} &= -0.012416467490;\ c_{1u} = 0.016661718438 \\ c_{2u} &= -1.970804881023;\ c_{3u} = 1.954143162584 \end{aligned}$$

Three point stencil for scheme B is given as,

$$a_{1c} f'_{i-1} + f'_i + a_{3c} f'_{i+1} + h\left(b_{1c} f''_{i-1} - b_{3c} f''_{i+1}\right) = \frac{1}{h}(c_{1c} f_{i-1} + c_{3c} f_{i+1}) \tag{15}$$

$$\frac{9}{8h}\left(f'_{i+1} - f'_{i-1}\right) - \frac{1}{8}\left(f''_{i+1} + f''_{i-1}\right) + f''_i = \frac{3}{h^2}\left(f_{i+1} - 2f_i + f_{i-1}\right) \tag{16}$$

The optimized coefficients in Eq. (15) are given as,

$$\begin{aligned} a_{1c} &= a_{3c} = 0.446675232769736 \\ b_{1c} &= b_{3c} = 0.065558410923245 \\ c_{1c} &= c_{3c} = 0.946675232769736 \end{aligned}$$

While analyzing numerical properties for schemes A and B, we have used the near-boundary stencils as given by Eqs. (9)–(12) to obtain f' and f'' at the respective nodes. We have considered a domain with 101 equi-spaced points for the purpose of analysis. For the central node of the domain, we have analyzed the effectiveness of the proposed CCD schemes in evaluating the first and second derivatives and compared these with the CCD schemes in [1,20].

In Fig. 1, discretization effectiveness for the central node has been shown by plotting the real and the imaginary parts of k_{eq}/k and $-k_{eq}^2/k^2$ versus non-dimensional wavenumber kh. Effectiveness in obtaining spectral resolution is shown by the variation of real part of k_{eq}/k versus kh. One can observe that the spectral resolutions of both the schemes A and B are higher as compared to the scheme of [20]. In all the four analyzed CCD methods, the scheme A has the highest spectral resolution and it outperforms the upwind CCD scheme suggested in [1]. The spectral resolution of scheme A remains close to the ideal limiting value of one almost up to $kh = 2.75$ as shown in Fig. 1a. Added numerical diffusion or anti-diffusion is represented by the negative or positive imaginary parts of k_{eq}/k respectively, and is shown in Fig. 1b. As proposed in [11,27], one can use upwind numerical methods to control the aliasing error in the high wavenumber components while performing LES. Thus to obtain a physically meaningful solution, the proposed method should have the numerical diffusion in the higher wavenumber range only. We have developed upwind scheme A in this aspect. From Fig. 1b one can observe that the scheme A is better as compared to the upwind scheme proposed in [1], since the added numerical diffusion is restricted more to the high wavenumber region. As the CCD scheme of [20] and scheme B have central stencils, these methods do not add any numerical diffusion.

Effectiveness of the proposed CCD schemes in estimating second derivative is shown in Fig. 1c by plotting the variation of the real part of $-k_{eq}^2/k^2$ versus kh. In [26], overshoot in real part of $-k_{eq}^2/k^2$ above one in high wavenumber region is advocated to eliminate numerical instabilities originating from aliasing error and other nonlinear effects. In Fig. 1c, one can observe the effectiveness of schemes A and B remains close to the ideal value of one over complete wavenumber range. The imaginary part of $-k_{eq}^2/k^2$ gives additional dispersion error, as discussed in [21]. For the central stencil of scheme B and CCD scheme of [20], this

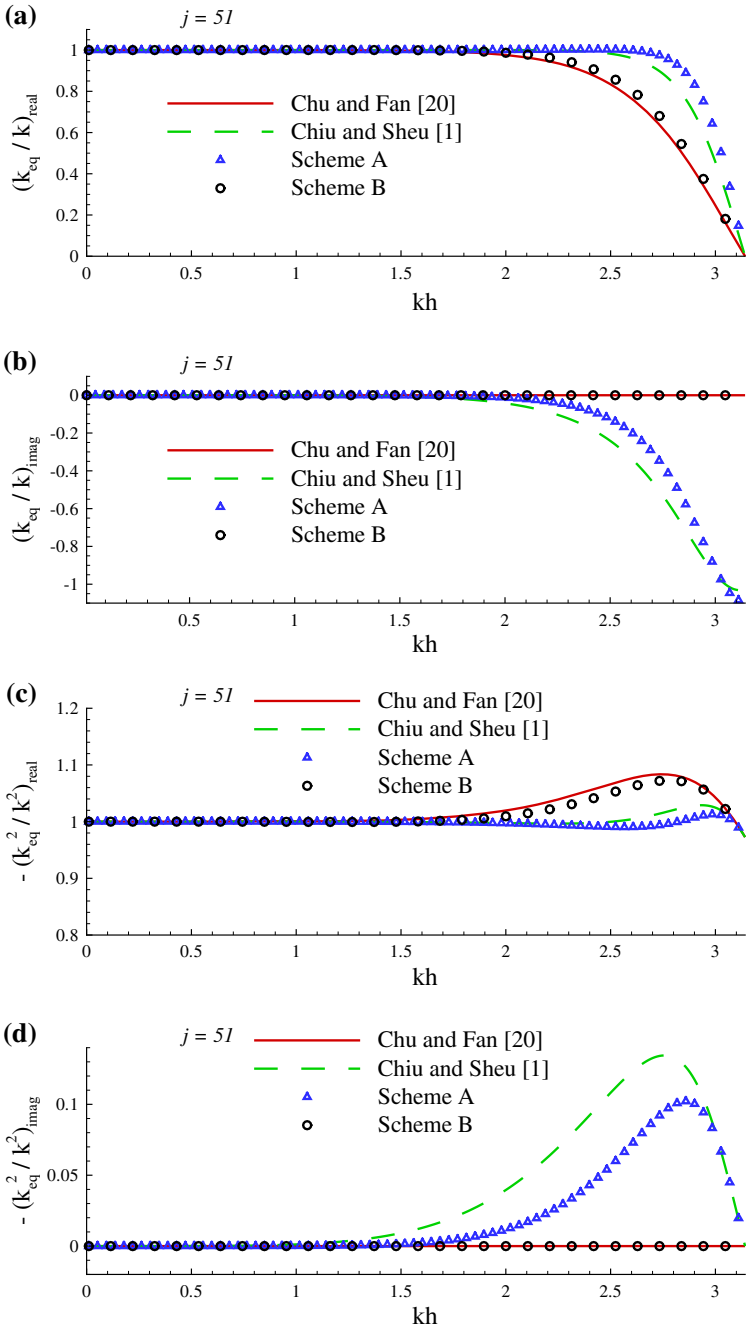

Fig. 1 Comparison of the effectiveness in evaluating the first and the second order derivative terms at the central node in the spectral plane. Here, k denotes the exact wavenumber while k_{eq} denotes the numerically obtained wavenumber while evaluating the first derivative. Similarly, the terms k^2 and k_{eq}^2 denote the exact and numerically obtained wavenumbers while evaluating the second derivative, respectively

quantity is zero while this error for the upwind scheme A is less as compared to the upwind CCD scheme proposed in [1].

Use of matrix spectral analysis allows us to calculate the nodal properties everywhere in the domain. Nodal properties are shown for the near boundary nodes $j = 2$ and $j = 100$ in Figs. 2 and 3, respectively. In these figures, one observes undesirable overshoot of the real part of k_{eq}/k above one for the CCD scheme of [20], but is absent for the schemes A and B for nodes $j = 2$ and $j = 100$. Additionally, the imaginary part of k_{eq}/k shows large numerical anti-diffusion for the node $j = 2$ and large diffusion for the node $j = 100$ for the CCD scheme of [20]. These problems are significantly reduced for the schemes A and B. Figures 2 and 3 also show that scheme A and scheme B outperform the CCD scheme of [20] in terms of the spectral resolution of the second derivative and the reduced additional dispersion error given by the real and imaginary parts of $-k_{eq}^2/k^2$, respectively. Thus Fig. 1 provides effectiveness while evaluating first and second derivatives at the interior nodes. Similar information is provided in Figs. 2 and 3 for the near boundary nodes. Use of different stencils at the boundary and near-boundary points causes significant variation in numerical properties such as spectral resolution, numerical amplification factor and numerical phase and group velocity [18,19]. Use of compact schemes sets up undesired directional bias in the computed solution and a symmetrization procedure has been suggested in [18,19] to avoid it. Thus use of proper discretization schemes for the boundary and near-boundary nodes is essential while performing LES and DNS studies as a choice of wrong boundary stencil can cause evolution of unphysical flow structures.

In [2,29], properties of the numerical schemes are analyzed by choosing 1D wave equation as the model equation for convection dominated flows with an emphasis on the numerical properties such as the numerical amplification factor $|G(k)|$, numerical phase speed $c_N(k)$, and numerical group velocity $V_{gN}(k)$. Similarly, we have analyzed the basic numerical properties of the CCD schemes. Ideally, for a chosen numerical method one requires neutral stability ($|G| = 1$) and zero phase and dispersion error. We consider the model equation for convection dominated flows as the following 1D convection equation,

$$\frac{\partial u}{\partial t} + c\frac{\partial u}{\partial x} = 0, \qquad c > 0 \tag{17}$$

Equation (17) has an analytical solution which can be used to make a direct comparison with the numerical results. Additionally, the initial condition given for solving this equation does not decay, amplify or disperse with time. Thus one can directly check the accuracy of a numerical scheme from the computed solution, whether there are dissipation and dispersion errors present in it or not.

For the analysis of 1D convection equation, consider the following initial condition for the numerical solution of Eq. (17),

$$u_m^0 = u(x_m, t = 0) = \int A_0(k)\, e^{ikx_m}\, dk \tag{18}$$

The general numerical solution for Eq. (17) is obtained by substituting the above initial condition in Eq. (17) as,

$$u_m^n = u(x_m, t^n) = \int A_0(k)\, (G_r^2 + G_i^2)^{n/2}\, e^{i(kx_m - n\beta)}\, dk \tag{19}$$

In Eq. (19), the numerical amplification factor $G(k)$ is defined as $G(k) = \frac{U(k,t^{n+1})}{U(k,t^n)}$ and is a complex quantity represented as $G(k) = G_r + iG_i$. Term β is obtained as $\tan\beta = -G_i/G_r$

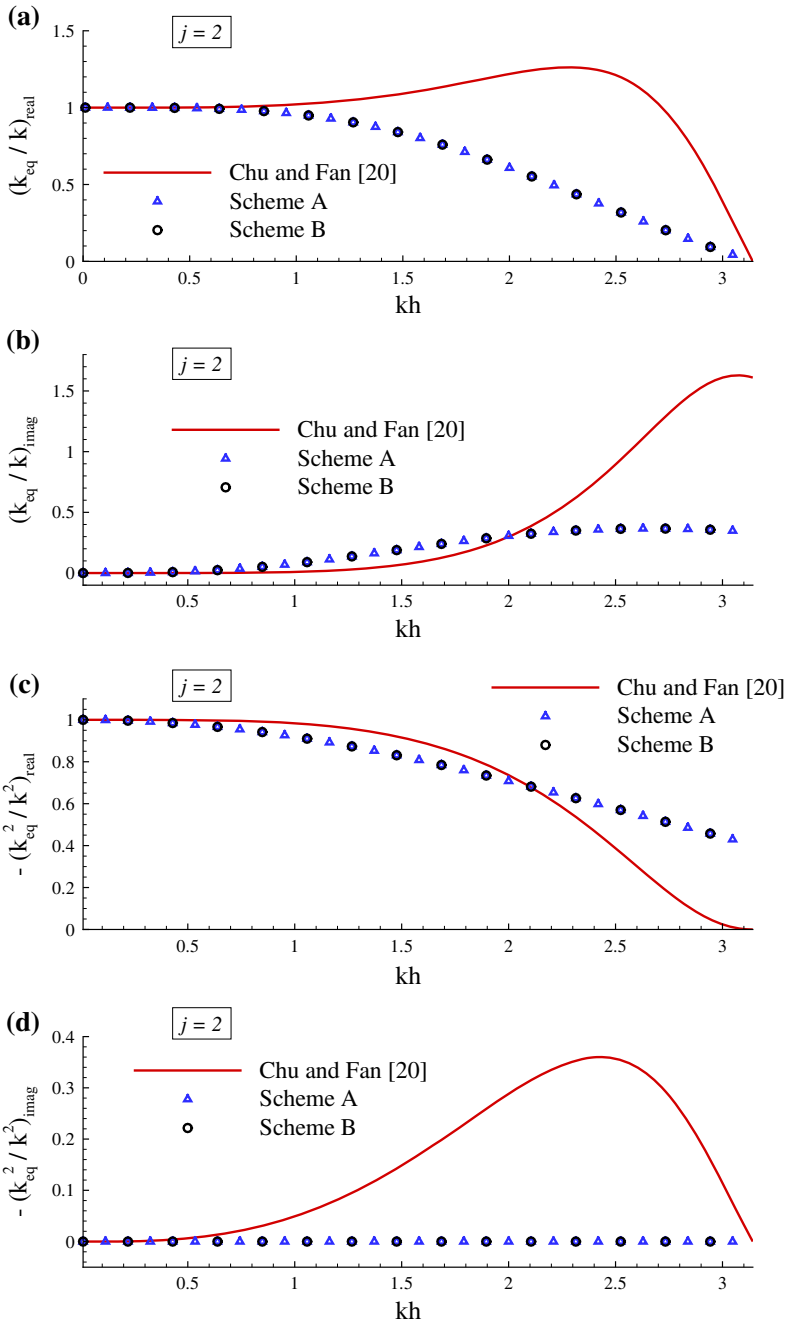

Fig. 2 Comparison of the effectiveness in evaluating the first and the second order derivative terms at the near-boundary node $j = 2$ in the spectral plane. Here, k denotes the exact wavenumber while k_{eq} denotes the numerically obtained wavenumber while evaluating the first derivative. Similarly, the terms k^2 and k_{eq}^2 denote the exact and numerically obtained wavenumbers while evaluating the second derivative, respectively

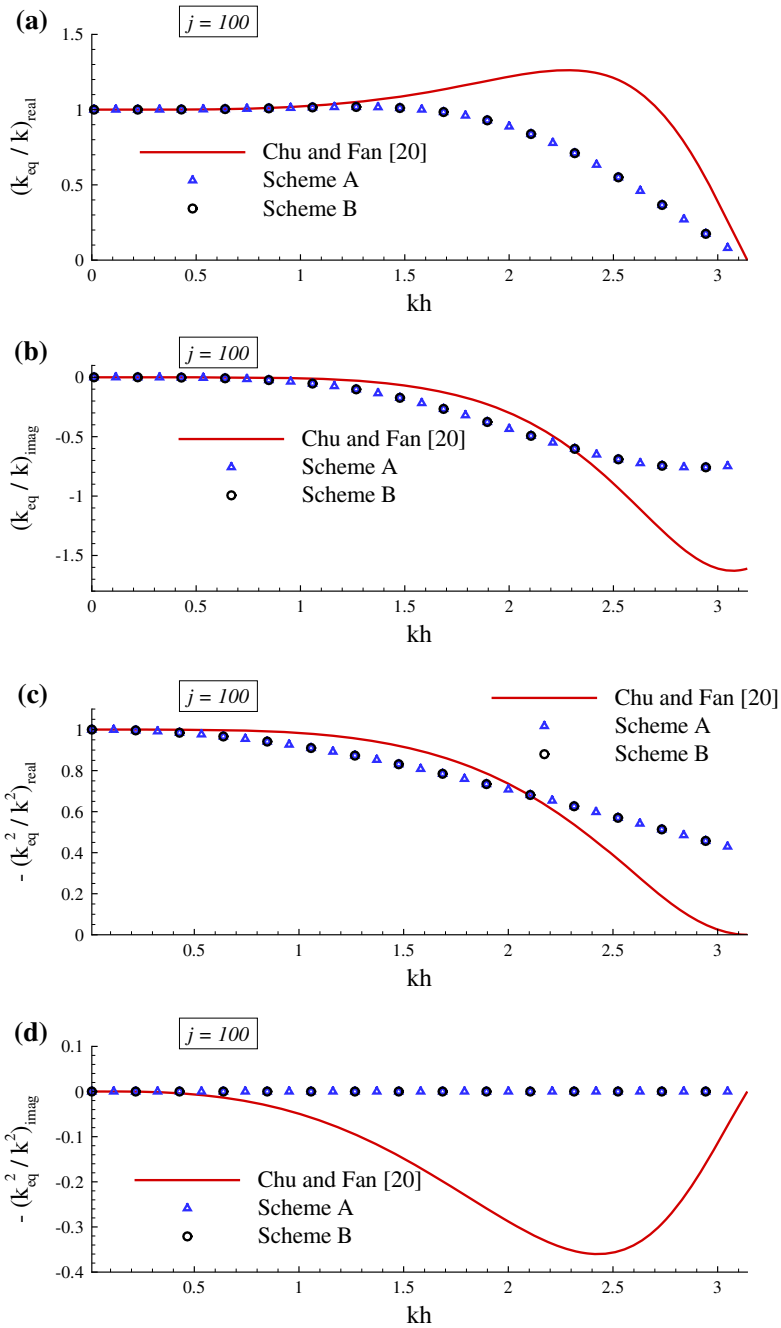

Fig. 3 Comparison of the effectiveness in evaluating the first and the second order derivative terms at the near-boundary node $j = 100$ in the spectral plane. Here, k denotes the exact wavenumber while k_{eq} denotes the numerically obtained wavenumber while evaluating the first derivative. Similarly, the terms k^2 and k_{eq}^2 denote the exact and numerically obtained wavenumbers while evaluating second derivative, respectively

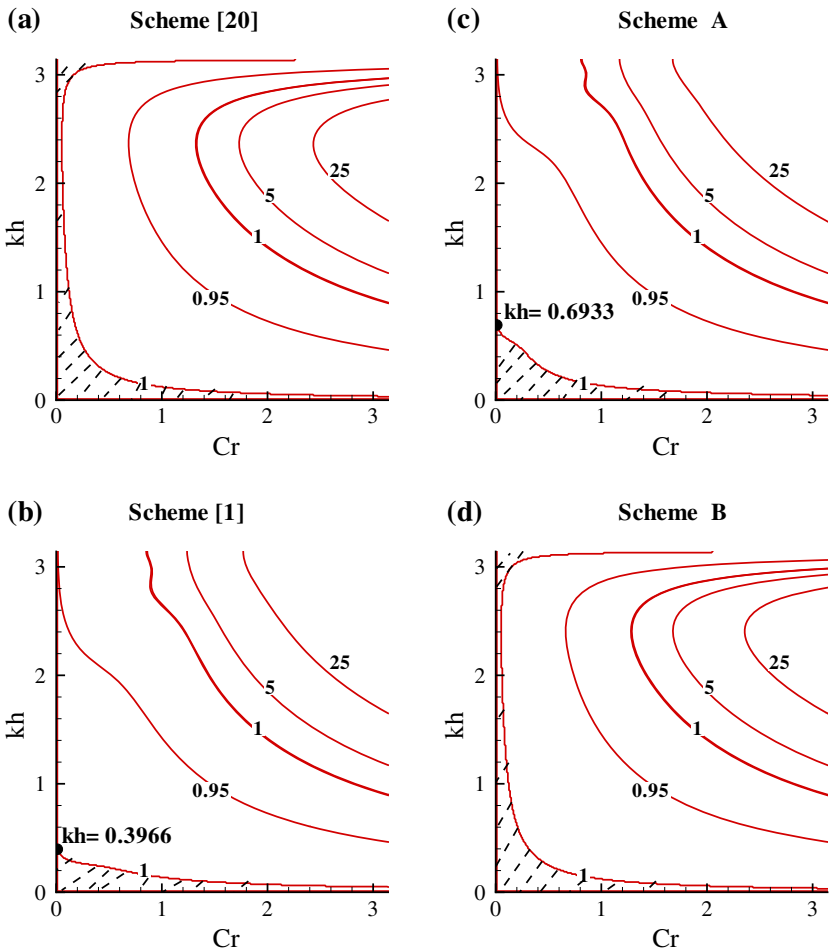

Fig. 4 Comparison of the numerical amplification factor $|G_j|$ contours for the central node corresponding to the solution of Eq. (17) when the indicated spatial discretization schemes are used with the fourth order Runge–Kutta (RK_4) scheme. Note that the areas hatched with *dashed lines* denote the neutrally stable regions

and is a function of wavenumber k. The numerical phase speed and numerical group velocity are obtained as [6,29],

$$\frac{c_N(k)}{c} = \frac{\beta}{\omega\,\Delta t} \tag{20}$$

$$\frac{V_{gN}(k)}{c} = \frac{1}{C_r h}\frac{d\beta}{dk} \tag{21}$$

where C_r denotes the CFL number.

We have analyzed these important properties for the central nodes. In Figs. 4 and 5, we have shown the numerical properties in (C_r, kh)-plane for the solution of Eq. (17) using the fourth-order Runge–Kutta RK_4 scheme for the time integration and the spatial discretization by the indicated CCD schemes. Figure 4 shows the comparison of variation of $|G|$ for the CCD schemes in [1,20] and the proposed schemes A and B. In these plots, we have highlighted the

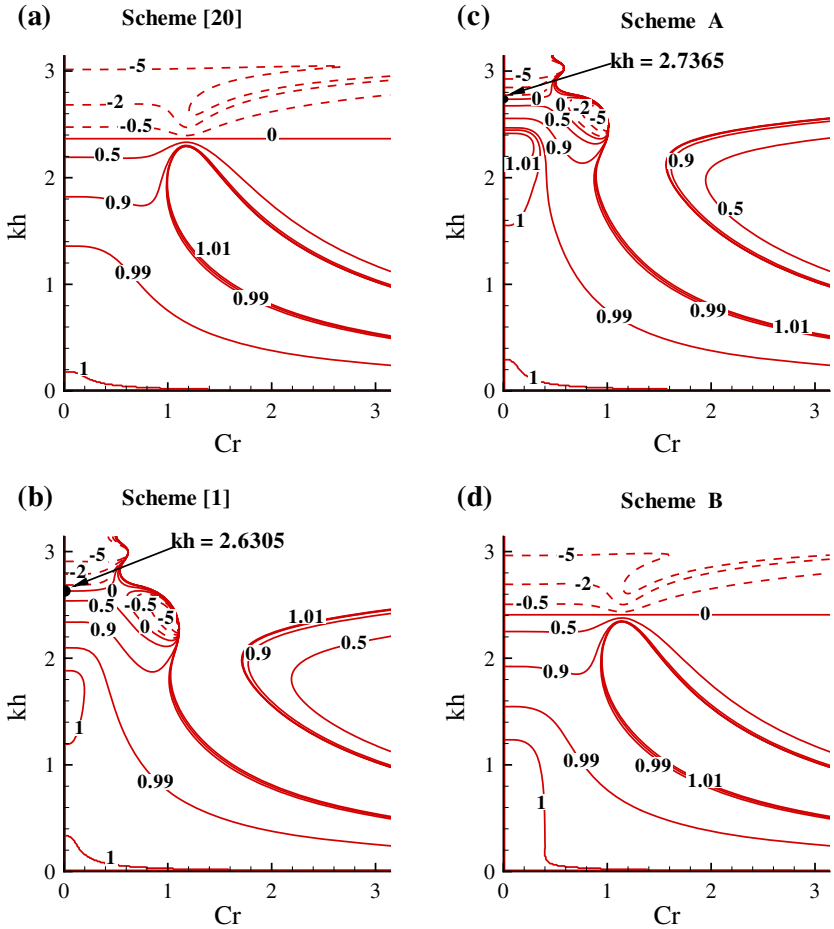

Fig. 5 Comparison of the numerical group velocity $|Vg_N/c|$ contours for the central node corresponding to the solution of Eq. (17) when the indicated spatial discretization schemes are used with the fourth order Runge–Kutta (RK_4) scheme. Note that the areas marked with *dashed lines* denote the q-wave regions with negative-valued group velocity

neutrally stable region by hatched lines to identify the suitable region for direct numerical simulation (DNS). Being a central scheme, proposed scheme in [20] and the scheme B have neutrally stable regions over a complete kh range for a small C_r values. Due to the upwind nature of the scheme A and the scheme in [1], neutrally stable region is limited to only low wavenumber range as marked in the respective frames with the corresponding wavenumber values. However the proposed scheme A has a higher neutrally stable region as compared to the scheme in [1] and is applicable to large eddy simulation (LES).

Figure 5 shows comparison of variation of V_{gN}/c in (C_r, kh)-plane for the numerical schemes discussed in Fig. 4 for the central nodes. Among all the four methods, scheme A has the best DRP properties. If one considers the area bounded by $V_{gN}/c = 0.99$ and $V_{gN}/c = 1.01$ contour lines as a DRP region then one obtains DRP region almost up to $kh = 2.5$ for scheme A as compared to $kh = 1.35$ for scheme in [20], $kh = 2.1$ for scheme of [1] and $kh = 1.55$ for the scheme B, when small C_r values are considered. Thus the

upwind scheme A has better DRP ability with respect to the upwind scheme of [1] and the central scheme B has a better DRP ability with respect to the central scheme of [20].

We have shown the negative group velocity contours by the dashed lines in this figure. Solution components in this range have a opposite direction of propagation as compared to the physical direction and are described as q-waves [30]. Such spurious high wavenumber oscillations can cause unphysical flow transition as well as numerical instabilities. Scheme A has the least q-wave region among the four methods and it exists only in the region where the solution is numerically damped. As indicated in the figure, for small CFL number calculations, q-wave region for scheme A starts from $kh = 2.7365$ as compared to $kh = 2.6305$ for the CCD scheme in [1]. For the central CCD scheme B and CCD scheme in [20], one observes a larger q-wave region above $kh = 2.4077$ and $kh = 2.3657$, respectively. For the scheme A, q-waves which are responsible for undesirable numerical artifacts are limited to very small (Cr, kh)-region which is significantly damped, thereby avoiding a need of upwind filters as suggested in [30].

Following the discussion on the numerical properties of the proposed CCD schemes, the efficiency of these proposed CCD schemes for the solution of model wave equations, as well as, Navier–Stokes equations is demonstrated in the next sections.

3 Solution of Wave Equation

Here, we report solutions of 1D and 2D wave equations corresponding to initial conditions with sharp gradient. We have reported and compared the numerical solutions for these problems obtained using the schemes A and B.

3.1 Solution of One-Dimensional Wave Equation with a Ramp Discontinuity

In many fluid flow and heat transfer problems, flow admits strong gradients of pressure, density and temperature. Capturing these sharp gradient events is computationally challenging since discontinuous solution in physical plane excites a complete band of frequencies in the spectral plane. Hence a numerical method with poor resolution will not correctly represent the physical solution with large dispersion and dissipation errors. Such poor numerical methods also show oscillating erroneous solution near discontinuities which is known as Gibbs' phenomenon. These high wavenumber oscillations are associated with the formation of q-waves which can lead to numerical instabilities [30]. Here, we will study this aspect by considering propagation of a steep ramp following the Eq. (17).

As an initial condition for this problem, we have specified the ramp function with a 81° slope, as shown in Fig. 6a, b. Numerical solution at subsequent times is prone to display a wide range of wavenumbers due to discontinuous slope in the initial condition. We have solved Eq. (17) with the schemes A and B using the RK_4 scheme for time integration.

We have considered a domain $0 \leq x \leq 30$, with 4096 equi-spaced points. Initially, the ramp is located between $x = 14$ and 15, as shown in Fig. 6a, b. While solving Eq. (17), we have chosen the phase speed $c = 0.5$ with a time step corresponding to the CFL number of 0.1. Along with the initial condition, numerical solutions computed using schemes A and B at $t = 3$ and 6 are shown in Fig. 6a, b, respectively. Amplitude of oscillating error generated near the ramp discontinuities is small as compared to the amplitude of ramp itself and these high wavenumber errors in the solution are not directly visible from the solutions shown in Fig. 6a, b. However, it is visible in Fig. 6c, d which show the errors between the analytical and the numerical solutions of Eq. (17) over the complete domain. Scheme A being an

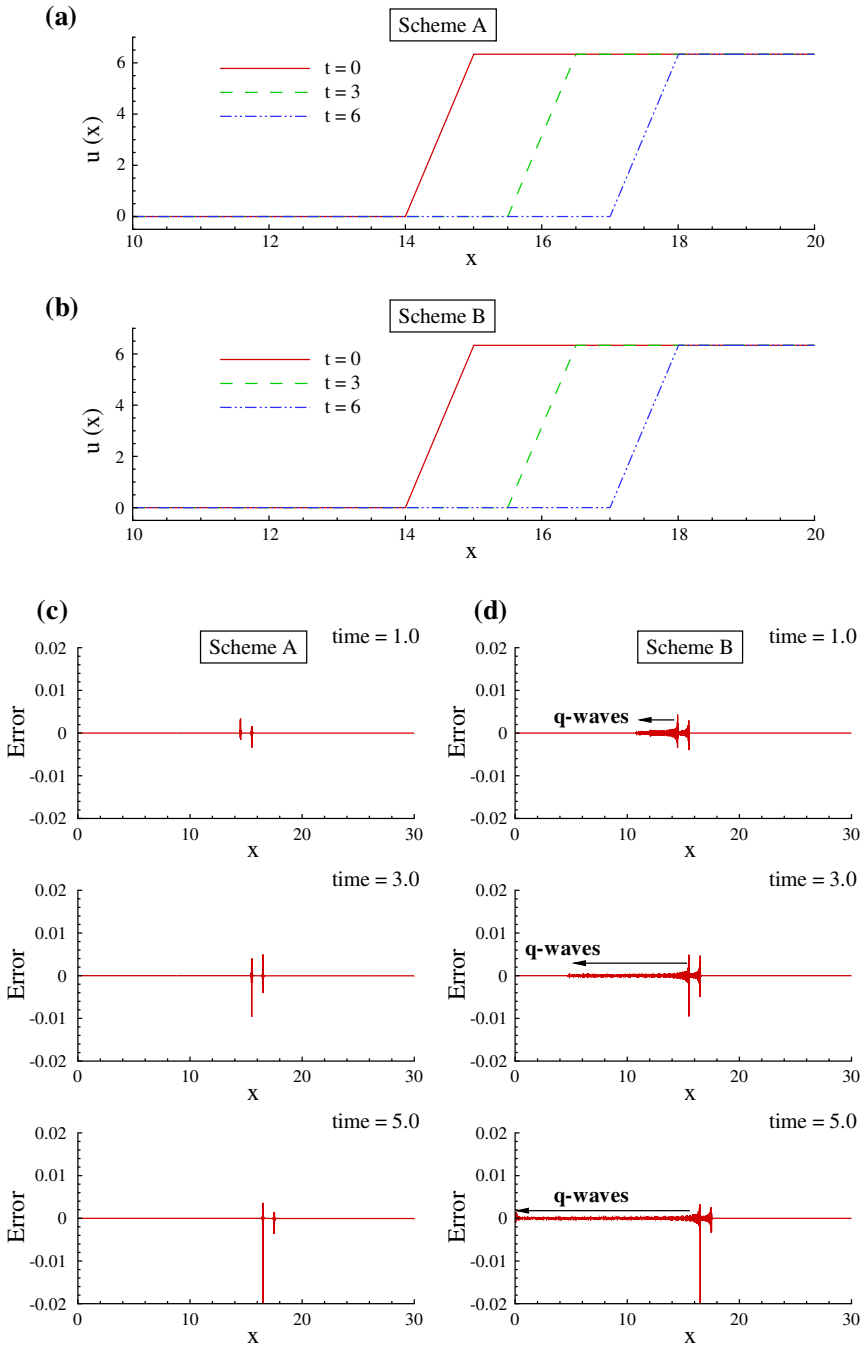

Fig. 6 Wave propagation profiles of a ramp function following Eq. (17) using the CCD scheme A and CCD scheme B have been shown in **a** and **b**, respectively. Error between the computed and the analytical solutions has been shown in **c** and **d** for the scheme A and scheme B, respectively

upwind scheme with a very small q-wave region (as seen from Fig. 5c), numerical solution in Fig. 6c shows only localized high wavenumber oscillations at the ramp discontinuities. There are no q-waves with significant amplitude at $t = 3$ and $t = 5$, as shown in Fig. 6c. However scheme B, being a central scheme with a small DRP region as compared to scheme A, admits q-waves in the solution as observed at $t = 3$ and $t = 5$ in Fig. 6d. Presence of these high wavenumber components in the numerical solution can have destabilizing effects and low-pass filtering is necessary, as suggested in [30]. However, computations performed with scheme A do not require this additional filtering due to its superior DRP properties, as well as the presence of numerical diffusion which is restricted to high wavenumber only. Thus for spatial discretization, use of scheme A is more beneficial.

3.2 Solution of Two-Dimensional Wave Equation with a Steep Wave Packet

Here, we have considered a model equation for 2D wave motion as,

$$\frac{\partial u}{\partial t} + c_x \frac{\partial u}{\partial x} + c_y \frac{\partial u}{\partial y} = 0 \tag{22}$$

In Eq. (22), c_x and c_y are the phase speeds in the x and y directions obtained using the expression $c_x = c \ \cos\theta$ and $c_y = c \ \sin\theta$, where θ is the angle between the direction of propagation of wave packet and the horizontal co-ordinate axis. In the current computational exercise, we have chosen a domain $0 \leq (x, y) \leq 6$, with 501 equi-spaced points with a grid spacing $h = 0.012$. We have specified a steep wave packet initially located at ($x_o = 1.5$, $y_o = 1.5$) following the equation,

$$u = e^{-500\left[(x-x_o)^2+(y-y_o)^2\right]} \ \cos\left[100\sqrt{(x-x_o)^2+(y-y_o)^2}\right] \tag{23}$$

moving along a line inclined at $\theta = 45°$ to x-axis. We have considered the phase speeds as $c_x = c_y = 0.1$ with a time step corresponding to the CFL number of $C_{rx} = 0.1$, where $C_{rx} = \frac{c_x \Delta t}{h}$.

We have compared solutions of this problem when the schemes A and B are used for spatial discretization and the RK_4 scheme is used for time integration, as shown in Fig. 7. The initial condition of the wavepacket is shown in Fig. 7a while the packet amplitude distribution along the line $y = 1.50$ is shown in Fig. 7b. In Fig. 7c, the results obtained using the scheme A at the indicated time instants are shown, while in Fig. 7d results obtained using the scheme B are shown. The choice of CFL number as $c_{rx} = c_{ry} = 0.1$ corresponds to the neutrally stable region over a complete wavenumber range for the scheme B shown in Fig. 4d. However, for scheme A such a neutrally stable region is limited to low wavenumber region only. Thus, the calculations obtained with scheme A shows subsequent damping of the wavepacket at the indicated times in Fig. 7. Results obtained using the scheme B show the presence of q-waves in the solution caused by the steep nature of the initial wave packet. As for the calculations obtained using the scheme B, even though the calculations are performed inside a neutral region, yet the peak amplitude of the wavepacket decreases with time. This reduction of the amplitude of the signal, despite performing calculations in the neutrally stable region, is due to the dispersion error as pointed out in Fig. 2 of [30].

We have solved an additional example of propagation of 2D wavepacket following Eq. (22) on a skewed grid to further demonstrate capabilities of proposed CCD schemes on a highly skewed grid. Grid plays important role in the numerical simulation. While dealing with complex geometries in real applications, many times researchers encounter skewed grids. This particular example is chosen to evaluate effects of highly skewed grids on the performance

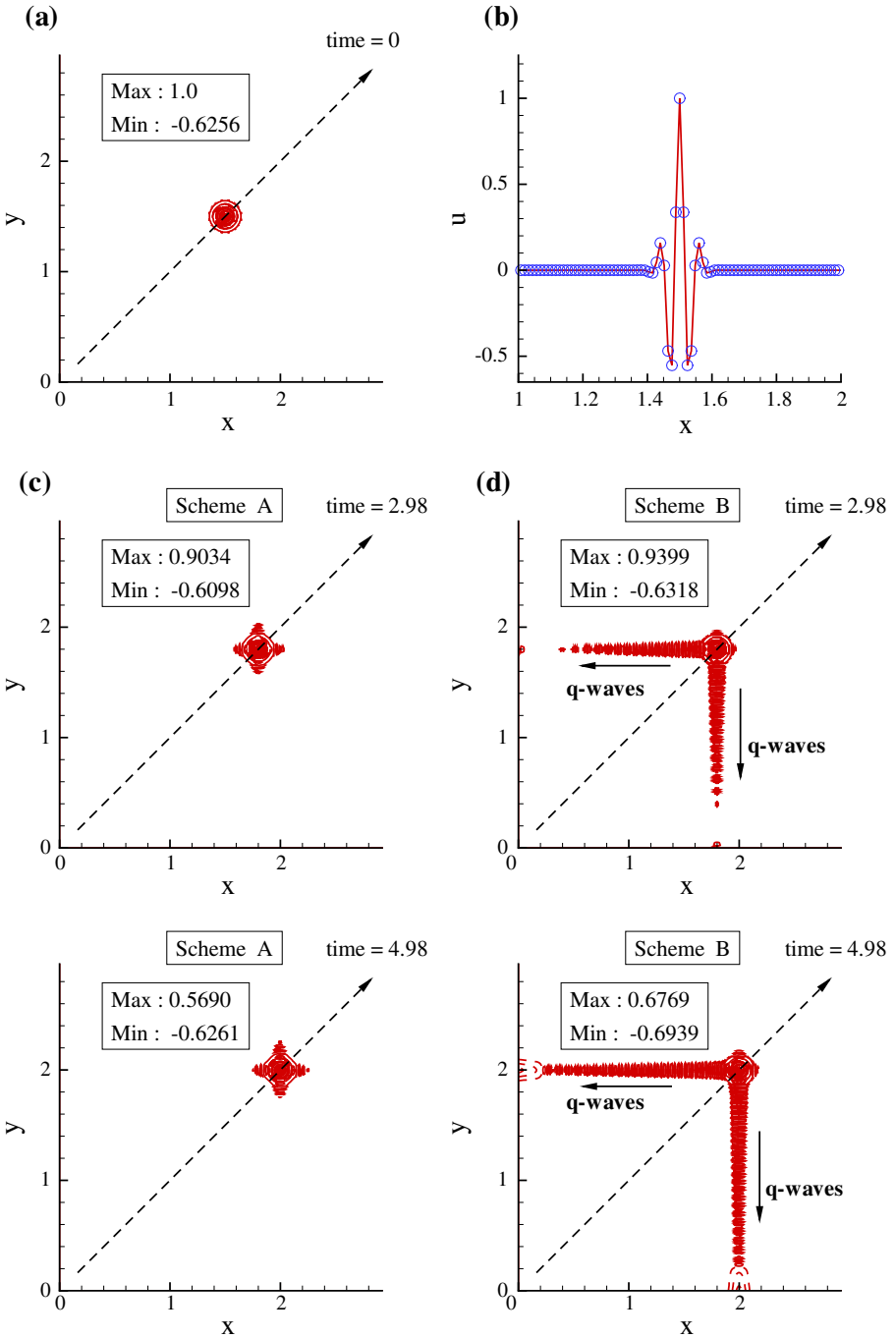

Fig. 7 Initial condition for the propagation of a steep wavepacket following Eq. (22) is shown in **a**, while the initial packet amplitude distribution along the line $y = 1.50$ is shown in **b**. Results obtained using the CCD scheme A and CCD scheme B have been shown in **c** and **d**, respectively. One can observe q-waves in the solution obtained using the central CCD scheme B

of proposed numerical schemes. Figure 8a shows the chosen domain and a wavepacket. The initial location of the wavepacket (x_0, y_0) is selected as the center of the domain. The wavepacket is given as

$$u = e^{-128\left[(x-x_o)^2+(y-y_o)^2\right]} \cos\left[\sqrt{(x-x_o)^2+(y-y_o)^2}\right]. \tag{24}$$

The packet is chosen to move along x-axis with a phase speed of $c_x = 1.0$ with a time step corresponding to the CFL number of $C_{rx} = 0.1$, where $C_{rx} = \frac{c_x \Delta t}{h}$. The domain has been divided into 501×501 grid points. The grid is highly skewed with a included angle between the $x, y = \text{ constant}$ lines is close to $11.31°$. Figure 8b, c show the computed solution using the proposed CCD schemes. One again observes significant reduction of q-waves for Scheme A as compared to Scheme B. The reason behind these results is clear from the Fast Fourier transform (FFT) of the solution amplitude on a $y = y_0$ line at $t = 1.5$ as shown in Fig. 8d. One observes that the high wavenumber components associated with the spurious q-waves in Fig. 5 are highly attenuated due to added numerical diffusion. One should also note that the amplitude of low wavenumber components for Scheme A is same as Scheme B, as the added numerical diffusion is significant only near the Nyquist limit. Thus, Scheme A attenuates high wavenumber components associated with q-waves and does not bring unphysical modification in low wavenumber components.

Thus, we list here the following three important conclusions drawn from the study of 1D and 2D wave equation problems.

1. For the space-time accurate numerical simulations, one should restrict the numerical calculations in the neutrally stable zone only.
2. Although a numerical scheme gives a neutrally stable region across the whole wavenumber range without providing correct dispersion relation at high wavenumbers, solution amplitude still decays as the q-waves draw energy from the main signal itself and thus attenuate the original signal.
3. The q-waves are spurious waves which give rise to unphysical events or result in numerical instability [30]. In order to get rid of these spurious waves one needs to use additional low-pass filter [30] or one can use a upwinding scheme like scheme A, which has the required numerical diffusion at high wavenumbers.

4 Discrete Vortex in a Uniform Flow

The presence of spurious waves is not only seen in the numerical solution of the model wave problems but also observed in the solution of Navier–Stokes equation. Here, we consider a problem regarding the convection of a discrete shielded vortex in a uniform flow. We have solved the Navier–Stokes equations using the proposed central and upwind CCD schemes. We have used a domain of size $-1 \leq (x, y) \leq 1$, with 512 equi-spaced points in the respective directions. As an initial condition, we have kept a discrete shielded vortex [32] close to the origin in a uniform flow. The schematic of this problem is shown in Fig. 9a. The flow domain is defined by a square region *ABCD* with an initial discrete vortex near the origin. As shown in this figure, flow enters the domain from the left boundary AB. One can prescribe a discrete shielded vortex as in [32]

$$\omega = K\ (1 - \beta\, r^2)\ e^{-\beta\, r^2} \tag{25}$$

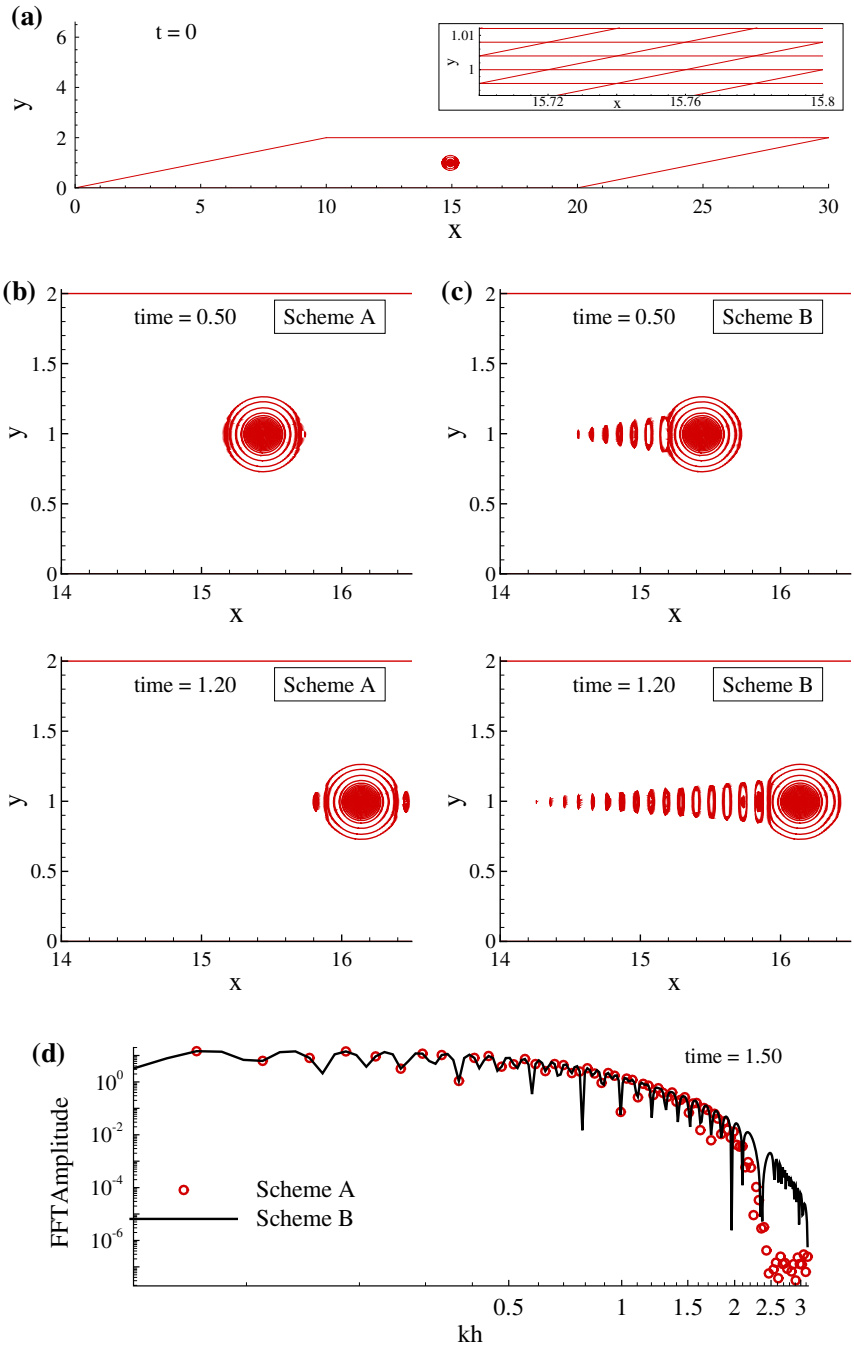

Fig. 8 Initial condition for the propagation of a wavepacket following Eq. (22) and chosen domain is shown in **a**. Results obtained using the CCD scheme A and CCD scheme B have been shown in **b** and **c**, respectively. FFT of the signal on a $y = y_0$ line at $t = 1.5$ is shown in **d**

Here, r is a distance between any point in the domain and the center of the vortex and is used to specify the initial vorticity distribution in the domain. Maximum amplitude at the center of the vortex is fixed by the parameter K which is chosen as 500 for the present simulations.

We have obtained solution of the Navier–Stokes equations following the formulation and methodology of [19], in the streamfunction—vorticity formulation. These equations in (x, y)-plane can be written in the transformed (ξ, η)-plane as

$$\frac{\partial}{\partial \xi}\left[\frac{h_{22}}{h_{11}}\frac{\partial \psi}{\partial \xi}\right] + \frac{\partial}{\partial \eta}\left[\frac{h_{11}}{h_{22}}\frac{\partial \psi}{\partial \eta}\right] = -h_{11}h_{22}\,\omega \tag{26}$$

$$h_{11}h_{22}\frac{\partial \omega}{\partial t} + h_{22}u\frac{\partial \omega}{\partial \xi} + h_{11}v\frac{\partial \omega}{\partial \eta} = \frac{1}{Re}\left[\frac{\partial}{\partial \xi}\left(\frac{h_{22}}{h_{11}}\frac{\partial \omega}{\partial \xi}\right) + \frac{\partial}{\partial \eta}\left(\frac{h_{11}}{h_{22}}\frac{\partial \omega}{\partial \eta}\right)\right] \tag{27}$$

where the parameters $h_{11} = \sqrt{(x_\xi^2 + y_\xi^2)}$ and $h_{22} = \sqrt{(x_\eta^2 + y_\eta^2)}$ are grid scale factors. As shown in Fig. 9a, we have prescribed a uniform flow at the inflow boundary AB. To update streamfunction and vorticity values at the rest of the boundaries BC, CD and DA, a convective outflow boundary condition [30] is applied on the normal component of the velocity vector. For the spatial discretization of convective and diffusion terms in Eq. (27), we have used either the scheme A or the scheme B. Dissipation terms in Eq. (26) are discretized using CD_2 scheme while we have used RK_4 time integration method for temporal discretization. Equations (26) and (27) are in non-dimensionalized form with the free-stream velocity U_∞ as a reference velocity scale and $1/K$ as the time scale. Thus the Reynolds number is defined as $Re = \frac{U_\infty^2}{\nu K}$. The present simulations are performed for $Re = 10^5$ with a time step of $\Delta t = 0.0001$.

We have chosen $\beta = 30{,}000$ and the initial vorticity distribution along the vortex center line ($y = 0.0019$) has been shown in Fig. 9b. Navier–Stokes solutions using the scheme A at different instants are shown in Fig. 9c while the results obtained using the scheme B are shown in Fig. 9d at the same instants. These frames show the zoomed view of the solution. As the flow direction is from left to right, vortex convects to the right direction along with the flow in subsequent time frames. We have marked the maximum and minimum values of the vorticity in the respective frames. Here, we have purposely chosen the higher value of $\beta = 30{,}000$ which gives rise to steep variation of the vorticity gradient in order to show the presence of q-waves. In the right column, computations performed with the scheme B show the left running q-waves while such spurious waves are not present in the left column corresponding to the results obtained using the scheme A. Thus the use of the scheme A is beneficial, as its solution does not show spurious q-waves, even for the solution of Navier–Stokes equations.

5 Flow Inside a Lid-Driven Cavity

Two-dimensional lid-driven cavity problem is a well known benchmark problem and has been the subject of many studies [1,21,31,33–36]. In this problem, fluid motion inside a square cavity is considered when the side and bottom walls are kept stationary, while the top surface moves with a uniform velocity. This problem has well defined domain as well as boundary conditions. We have first calibrated our results obtained from the schemes A and B by comparing with the results in the literature [1,21,31,33–35]. Results for a steady state solution observed at $Re = 1{,}000$ have been compared with the previous studies while the efficiency of scheme A has been shown from its de-aliasing nature observed for an unsteady flow at $Re = 10^4$. We have used a grid with 301 equi-spaced points in both directions and

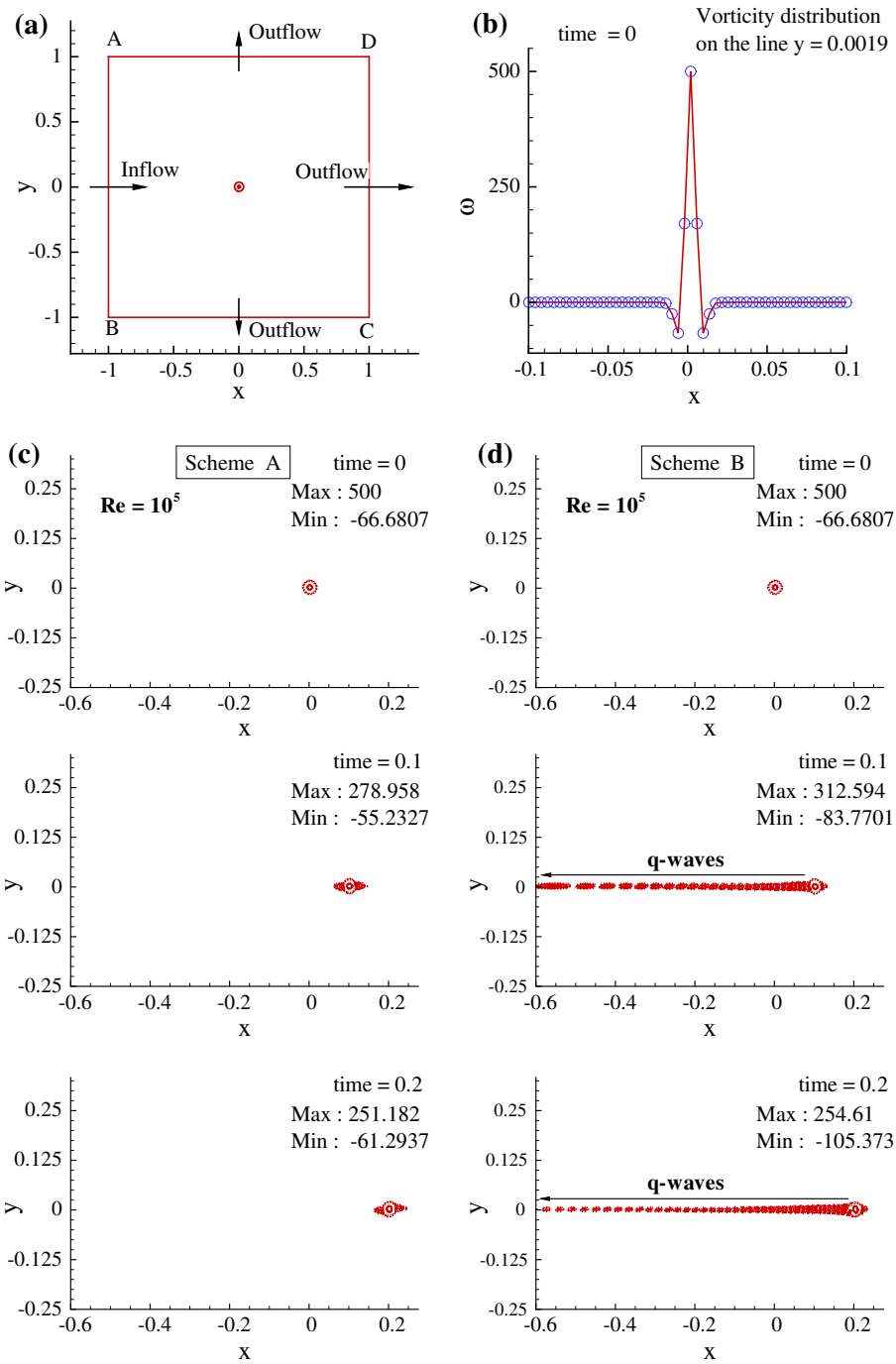

Fig. 9 **a** Schematic of the propagation of a steep discrete vortex in a uniform flow following Eqs. (26) and (27); **b** vorticity distribution along the centerline $y = 0.0019$ of the domain; numerical simulation results using the CCD scheme A and CCD scheme B have been shown in **c** and **d**, respectively. One can observe q-waves in the solution obtained using the central CCD scheme B

the calculations are performed with a time step of 0.001. We have used the discretization methodology of Navier–Stokes equations as discussed for the problem of the discrete vortex in uniform flow in the last section.

In Fig. 10, we have compared the streamfunction contours for $Re = 1{,}000$ obtained using the proposed CCD schemes with results in [33]. The contours correspond to the steady state condition which is defined as the solution corresponding to the condition of $(\frac{\partial \omega}{\partial t})_{max} < 10^{-9}$. For this Reynolds number, Ghia et al. [33] identified a central rotating eddy as a primary eddy P. Additionally, there are two eddies at the left and right bottom corners of the cavity which are identified as the corner eddies BL and BR. From Fig. 10, one can observe a good qualitative match between the results computed using the proposed CCD schemes and the results provided in [33]. The predicted region of the left and right corner vortices in the present computations is same as in [33] and Fig. 10 gives us a good qualitative match with previously published result.

However, a quantitative match is also essential and we have given the maximum and minimum values of stream function for $Re = 1{,}000$ obtained by different researchers in Table 1. The values of the maximum and minimum streamfunctions for the present computations are in a close match with the results of Bruneau and Saad [35] obtained on the grid of size $(1{,}024 \times 1{,}024)$ and the highly accurate results of Botella and Peyret [34] obtained using the Chebyshev collocation method. This highlights the efficiency of the proposed schemes for solving this flow problem. Comparison of the predicted eddy centers of the primary eddy P and the corner eddies BL and BR along with the vorticity values at the center of eddies is shown in Table 2 for $Re = 1{,}000$. Once again, one observes a close match between the computed results and the results available in the literature. Further, we have shown the variation of the velocity component u in the direction of lid motion and the component v perpendicular to the direction of lid motion at the geometric center of the lid driven cavity in Fig. 11. The present computational results obtained using the CCD schemes A and B are in close match with the results in [33].

We have further compared the results for lid driven cavity flow in Fig. 12 which are obtained using the proposed CCD schemes for $Re = 10{,}000$. Unlike the steady flow field results shown for $Re = 1{,}000$, numerical solution of lid driven cavity flow for $Re = 10{,}000$ has unsteady nature as shown in [22]. Presence of a weak triangular vortex structure was reported at the center of the cavity for this Reynolds number case [22]. Existence of this triangular vortical structure was attributed to the use of high accuracy numerical schemes which control level of background numerical disturbances along with the numerical error associated with dissipation and dispersion. Present calculations have captured similar triangular vortex which has also transient nature. In [22], three primary vortices gyrating around the central triangular vortex P were identified as satellites ($S1$, $S2$, $S3$). Additionally, secondary vortices ($SS1$, $SS2$, $SS3$) along with the three sets of corner vortices ($C1$, $C2$, $C3$) were observed. In Fig. 12, we have marked similar vortical structures corresponding to the results obtained using proposed CCD schemes. Due to the higher resolving ability of the present schemes, triangular vortical structure at the center of the cavity along with the primary and secondary satellite structures have been resolved accurately.

In [22], the computed lid driven cavity results for this Reynolds number were analyzed from the view point of aliasing error. It was found that, the overshoot of the second derivative discretization effectiveness for the CCD scheme of [20] near the high wavenumber region helps in de-aliasing the numerical solution. However, it was also found that when the same CCD scheme was used to solve the problem of receptivity in boundary layer, aliasing problem becomes serious outside the shear layer. As a remedy to this problem, modification of the convection terms using the upwinding concept was suggested in [22].

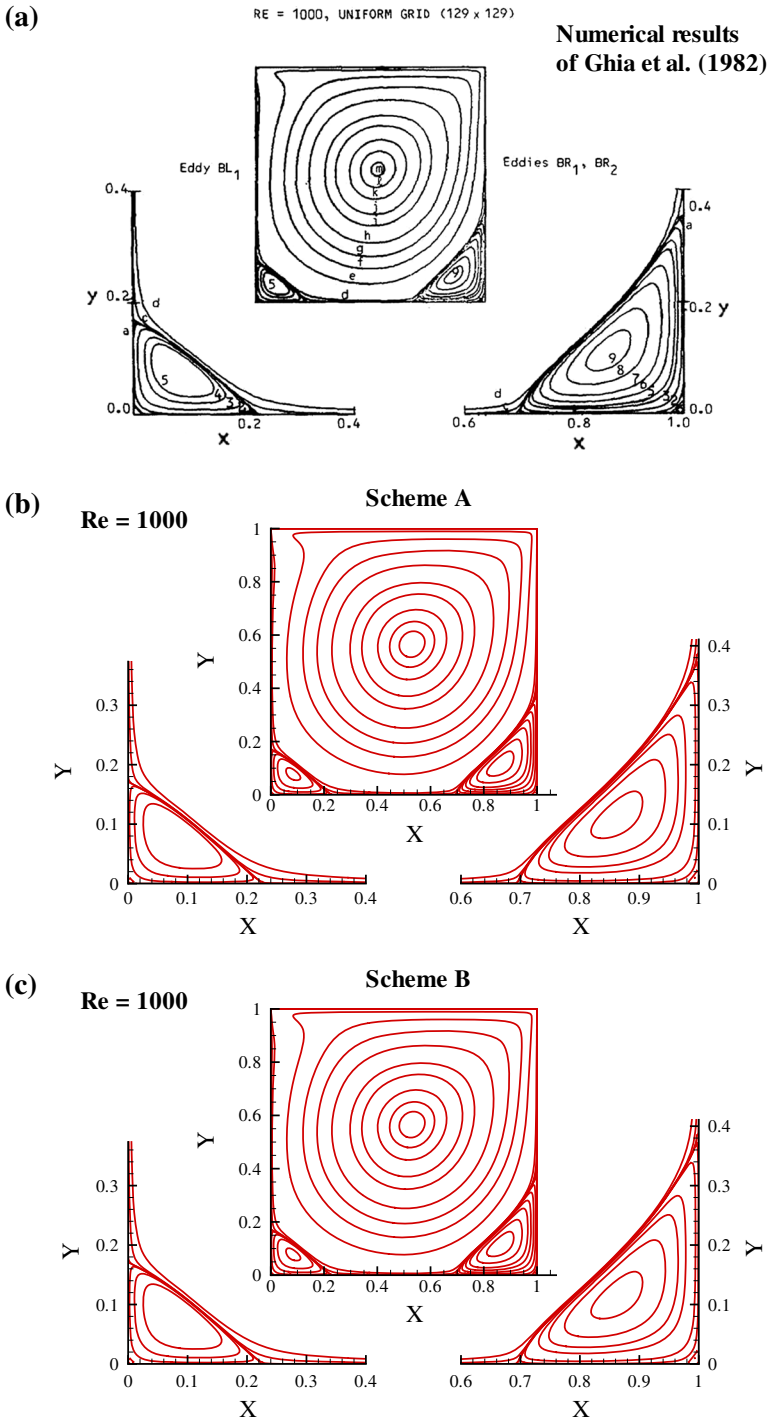

Fig. 10 Comparison of the predicted streamfunction contours for the lid driven cavity flow at $Re = 1{,}000$ using the scheme A and the scheme B with the results of Ghia et al. [33]

Table 1 Maximum and minimum values of streamfunctions for $Re = 1{,}000$

S. No	Methods and grids	ψ_{max}	ψ_{min}
1	CCD scheme A (301 × 301)	0.118692	-1.76008×10^{-3}
2	CCD scheme B (301 × 301)	0.11869	-1.76×10^{-3}
3	Botella and Peyret [34] (N = 160)	0.1189366	-1.729717×10^{-3}
4	Bruneau and Saad [35] (1,024 × 1,024)	0.11892	-1.7292×10^{-3}
5	Ghia et al. [33] (129 × 129)	0.118735	-1.74562×10^{-3}
6	Sengupta et al. [21] (257 × 257)	0.118908	-1.72577×10^{-3}

Table 2 Comparison of predicted eddy centers (primary eddy P, corner eddies BL and BR) and vorticity values at the center of eddies for $Re = 1{,}000$

Eddy type	Methods and grids	Center of the eddy	ω
Primary eddy (P)	CCD scheme A (301 × 301)	0.5302, 0.5660	2.06614
	CCD scheme B (301 × 301)	0.5303, 0.5659	2.0661
	Botella and Peyret [34] (N = 160)	0.5308, 0.5652	2.067753
	Sheu and Chiu [31] (129 × 129)	0.5311, 0.5637	–
	Ghia et al. [33] (129 × 129)	0.5313, 0.5625	2.04968
Corner eddy (BL)	CCD scheme A (301 × 301)	0.0835, 0.0773	−0.346663
	CCD scheme B (301 × 301)	0.0834, 0.0773	−0.345295
	Botella and Peyret [34] (N = 160)	0.0833, 0.0781	−0.3522861
	Sheu and Chiu [31] (129 × 129)	0.0850, 0.0776	–
	Ghia et al. [33] (129 × 129)	0.0859, 0.0781	−0.36175
Corner eddy (BR)	CCD scheme A (301 × 301)	0.8633, 0.1131	−1.1195
	CCD scheme B (301 × 301)	0.8634, 0.1131	−1.1193
	Botella and Peyret [34] (N = 160)	0.8640, 0.1118	−1.109789
	Sheu and Chiu [31] (129 × 129)	0.8626, 0.1105	–
	Ghia et al. [33] (129 × 129)	0.8594, 0.1094	−1.15465

Here, we have computed the same lid driven cavity problem for $Re = 10{,}000$ to check whether the solutions of CCD schemes A and B display aliasing error. The top frames (a) and (b) of Fig. 13 show the streamfunction contours at $time = 250$ for the schemes A and B, respectively, while the corresponding zoomed views near the top right corner are shown in Fig. 13c, d, respectively. The streamfunction contours for the scheme B show high wavenumber oscillations near the top corner while the contours for the scheme A do not show such oscillations. Solution for the scheme A is smooth as compared to the solution obtained from the scheme B. This is due to the upwind nature of scheme A. Fast Fourier transform of the vorticity data obtained on the second last horizontal line near the top surface for scheme B shows rise in amplitude near the Nyquist limit. This attribute suggests the scheme B is very much prone to aliasing error as pointed out in [22]. While the FFT for the results of scheme A do not show the rise in tail amplitude. Thus the upwinding nature of scheme A helps in de-aliasing the numerical solution as predicted in [11,22]. Hence the scheme A has both the desirable features; DRP property as well as de-aliasing nature.

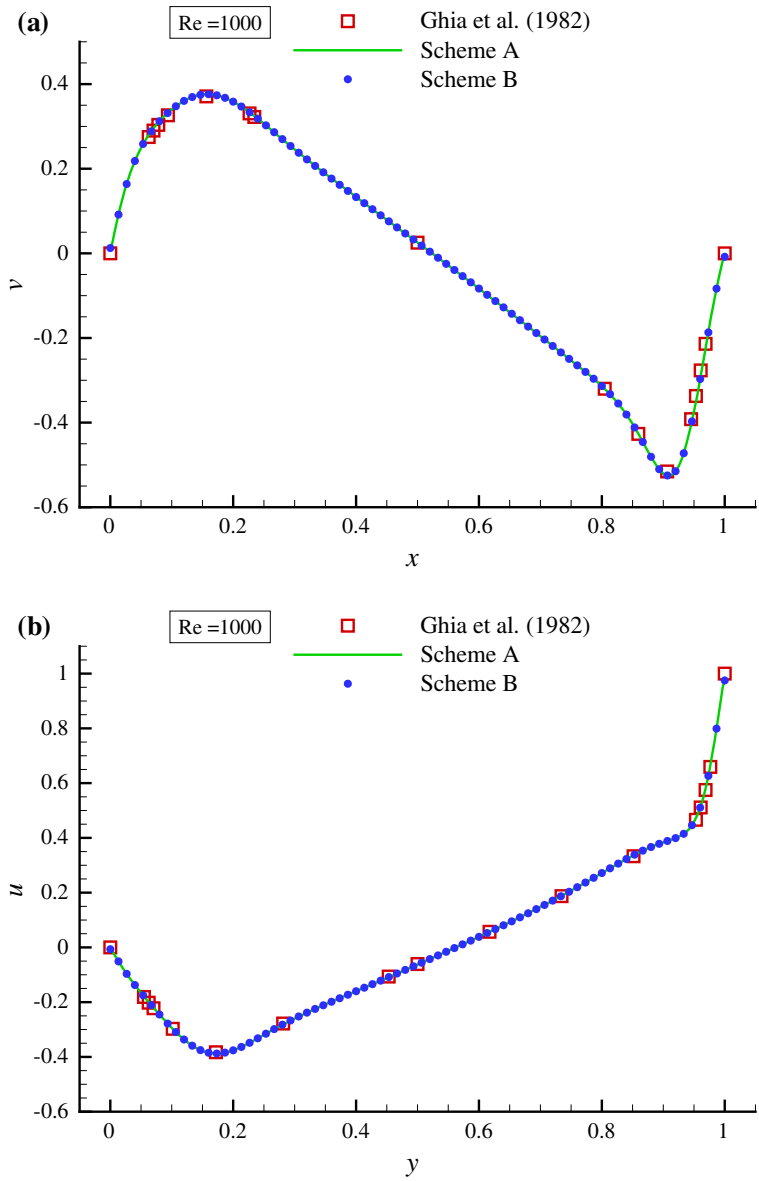

Fig. 11 Comparison of u and v components of the velocity vector at the geometric center of the lid driven cavity for the flow investigated at $Re = 1{,}000$

We have further applied the proposed optimized CCD Scheme A to solve the flow inside a three-dimensional cavity. Schematic of the three-dimensional cavity flow problem has been shown in Fig. 14. Geometry of the cavity is considered as a cube of unit dimension. For the sake of computational efficiency, the incompressible Navier–Stokes solutions are carried out by the divergence free condition (DFC) compensated method [31]. The viscous incompressible flow equations which include the continuity and momentum equations have been cast in the

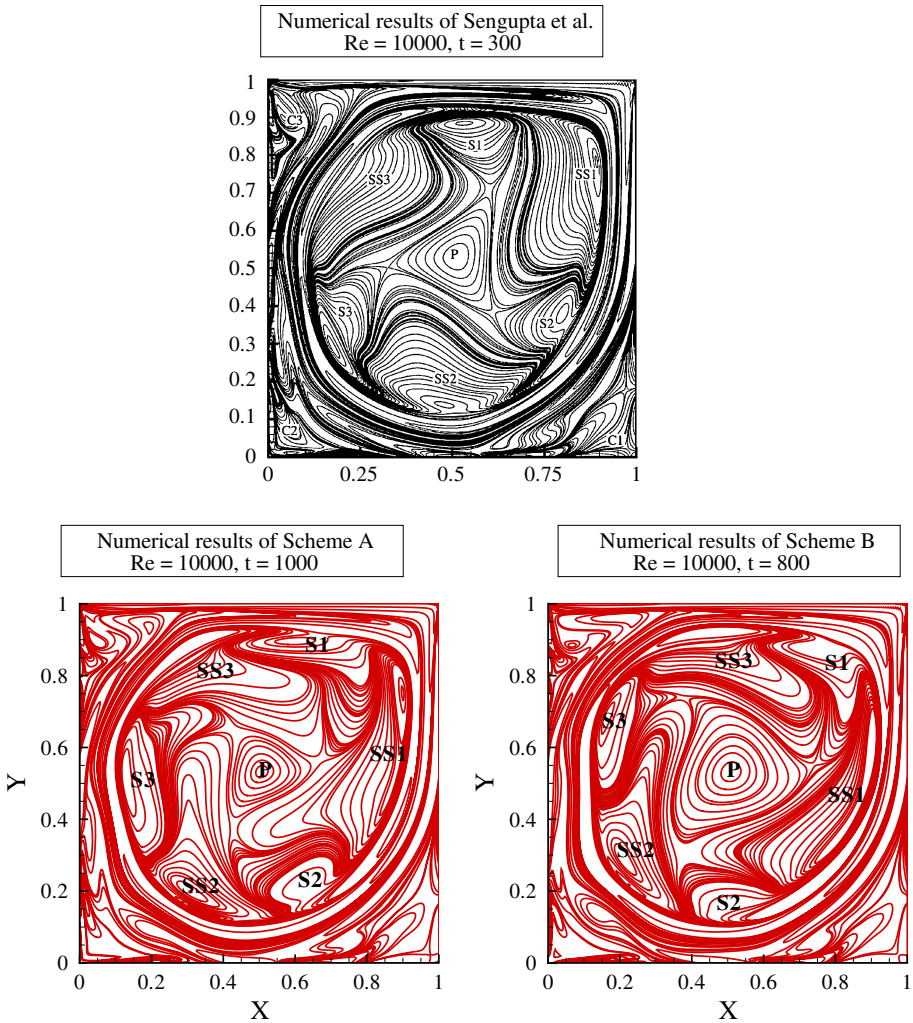

Fig. 12 Comparison of the vorticity contours for the lid driven cavity flow at $Re = 10{,}000$ using the scheme A and the scheme B with the results of Sengupta et al. [22]

primitive-variable pair $(\underline{u}, p)$ form and are solved corresponding to the Reynolds number Re as

$$\nabla \cdot \underline{u} = 0. \tag{28}$$

$$\frac{\partial \underline{u}}{\partial t} + (\underline{u} \cdot \nabla)\, \underline{u} = -\nabla p + \frac{1}{Re} \nabla^2 \underline{u}, \tag{29}$$

In this flow inside a three dimensional lid driven cavity example, we have reported numerical solutions for three different Reynolds number using two different $(41 \times 41 \times 41)$ and $(61 \times 61 \times 61)$ grid sizes. We have purposefully kept the grid size coarser in order to demonstrate the capabilities of the proposed numerical scheme. The velocity profiles of u

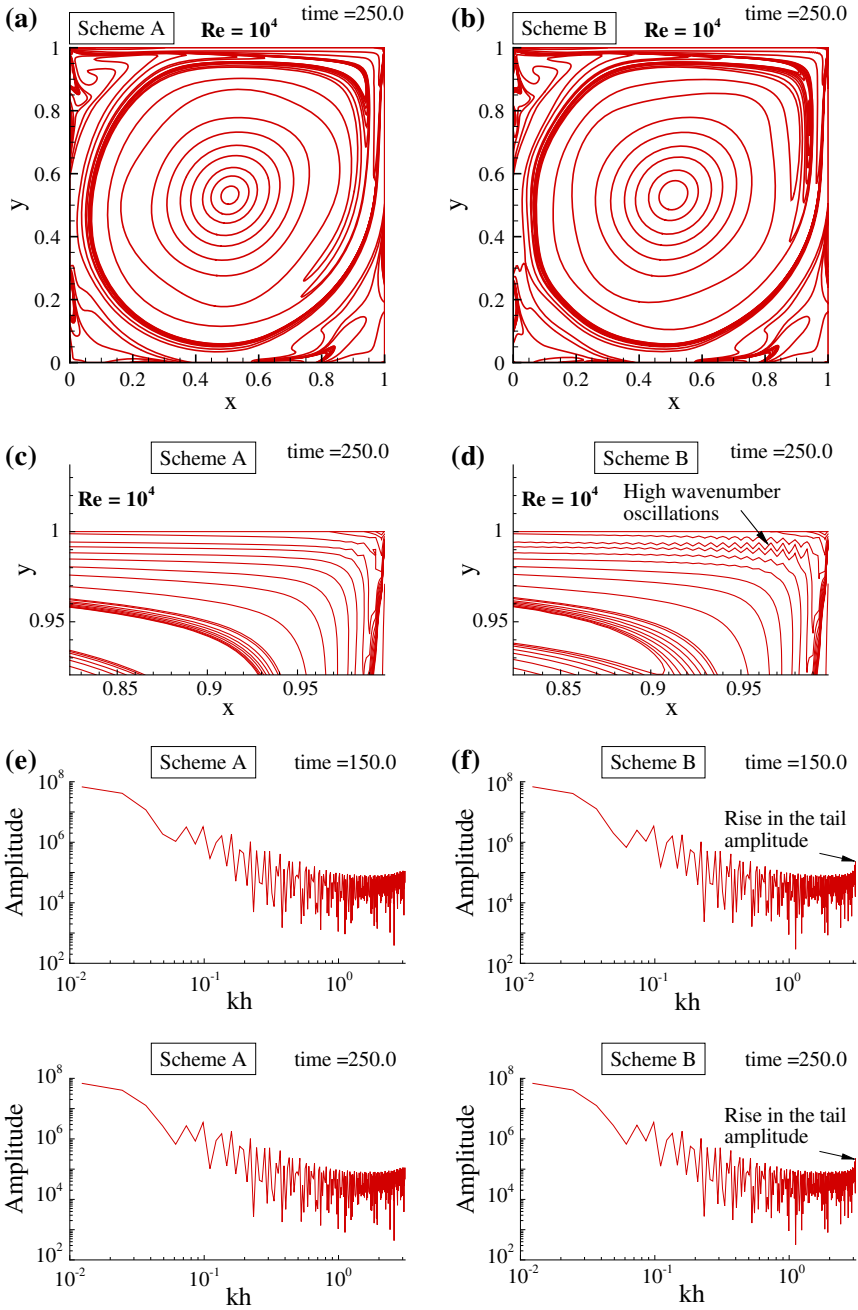

Fig. 13 Comparison of streamfunction contours for the lid driven cavity flow for $Re = 10^4$ at the indicated instant shown for the scheme A and the scheme B in **a** and **b**, respectively, while **c** and **d** show the zoomed view of **a** and **b**, respectively. One can observe the presence of high wavenumber oscillations in the solution obtained using the scheme B near the top right corner. FFT of the vorticity data along the line $y = 0.99666667$ is shown for the schemes A and B in **e** and **f**, respectively, at the indicated instants. Scheme B results show rise in the tail amplitude and are more prone to the aliasing error

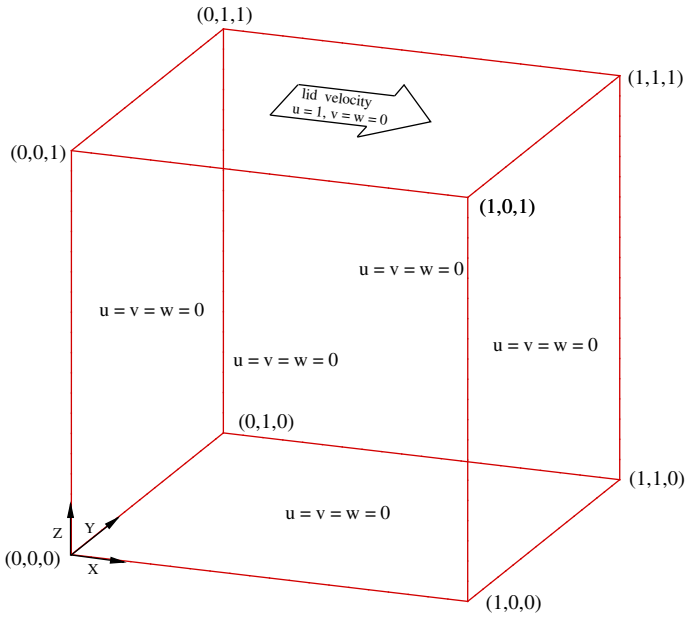

Fig. 14 Geometry of lid-driven flow in a cubic cavity

component along the vertical centerline and w component along the horizontal centerline of the plane $y = 0.5$ are plotted in Fig. 15 for $Re = 100,\ 400$ and $1{,}000$, respectively. It can be seen that the velocity profiles agree very well with the results in Lo et al. [41]. In addition, two-dimensional planar projections of the velocity vector field at $Re = 100$, 400 and 1,000 on the plane is shown in Fig. 16. It can be observed from the stream function in the plane of $y = 0.5$ that the axis of the primary vortex starts in the upper right half region, then gradually moves towards the cube center as the Reynolds number increases. One can also clearly see from Fig. 16 that the predicted stream function contours on mid-planes at $y = 0.5$ are similar to those in [42].

6 Simulation of Decaying Two-Dimensional Turbulence in a Square Container

We have further obtained solution of the Navier–Stokes equations in streamfunction-vorticity formulation as given by Eqs. (26) and (27) using the proposed CCD Scheme A to solve a 2D decaying turbulence problem. We have considered a solid square container with a geometry $(-1 \leq x, y \leq 1)$ containing fluid. The domain has been divided into 1,024 equi-spaced points in both the directions. For the present computation a time step of 5×10^{-4} has been used. As an initial condition, 16 nearly equal sized Gaussian vortices with a dimensionless radius of 0.10 are randomly located close to central region of the domain, away from the solid walls as shown in the top left frame of Fig. 17. Positive circulation has been assigned to the half of the vortices while for the remaining vortices have been given negative circulation. Prescription of these vortices induces velocity field through out the domain. In order to ensure a no slip condition at the domain boundaries for the prescribed initial condition, we have used smoothing function on vorticity distribution as used in [38]. This smoothing function

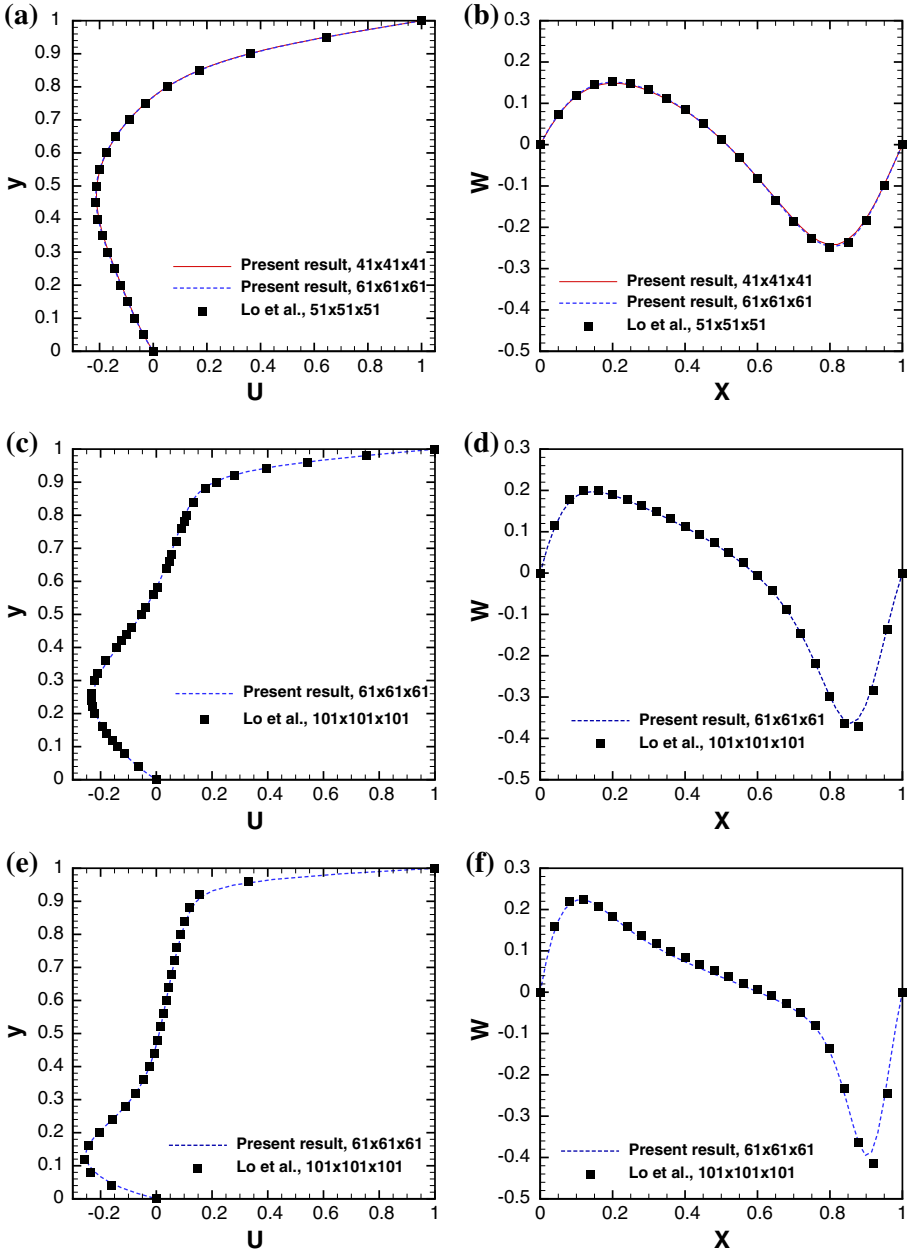

Fig. 15 Velocity profile for $Re = 100, 400$ and $1{,}000$ on vertical and horizontal centerlines at $y = 0.5$: **a** and **b** Re $= 100$, **c**, **d** Re $= 400$, **e**, **f** Re $= 1{,}000$

forces no-slip condition at the walls of the solid container. Initially, magnitude of amplitude of individual vortices is kept close to 150. With this initial condition and chosen domain, we have solved the flow field corresponding to a Reynolds number of $Re = 2{,}000$. Reynolds number is based on the characteristic velocity scale U which is a RMS velocity of the initial

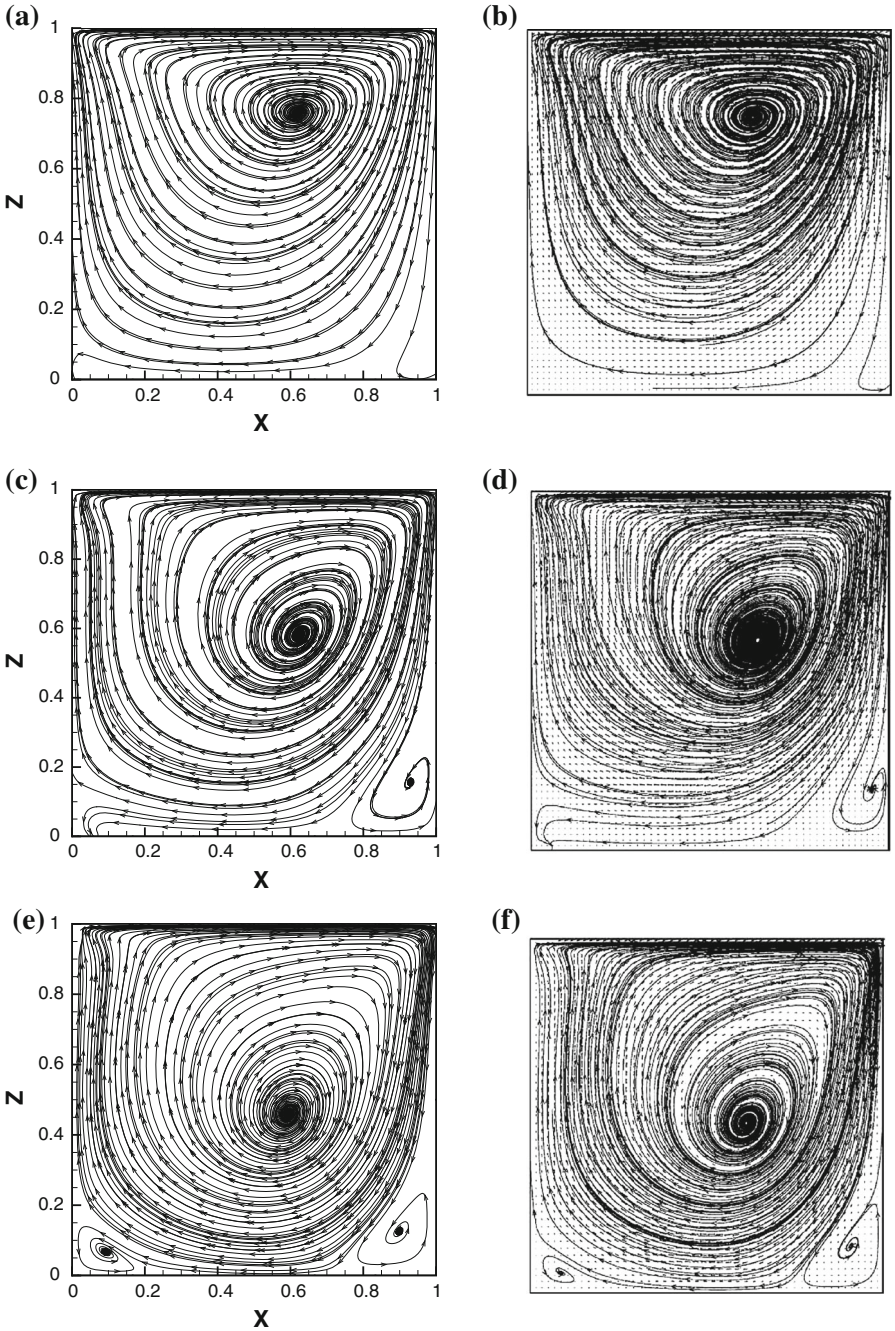

Fig. 16 Stream function on mid-planes at $y = 0.5$: **a** Re = 100, **b** Re = 100 [42], **c** Re = 400, **d** Re = 400 [42], **e** Re = 1,000, **f** Re = 1,000 [42]

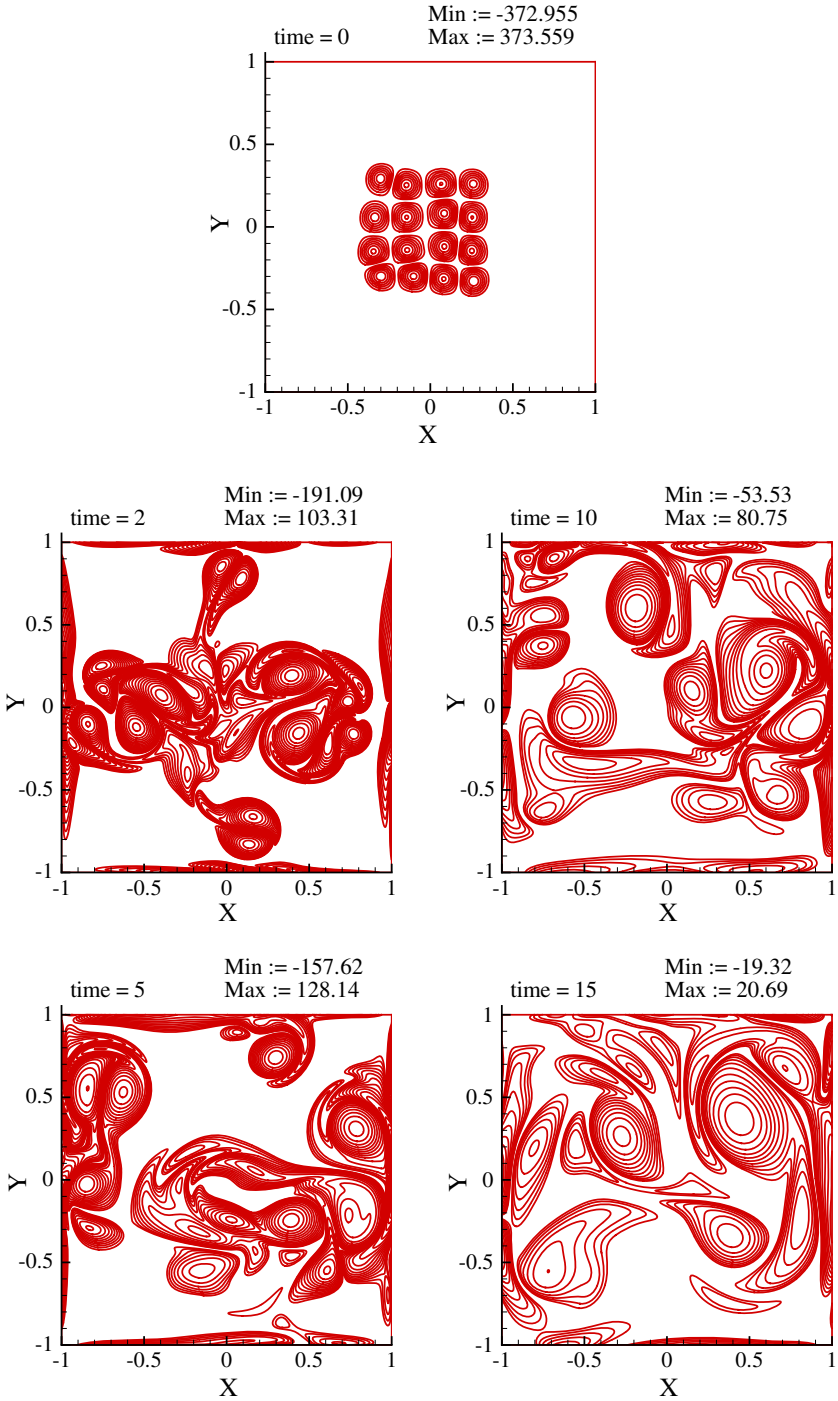

Fig. 17 Vorticity contour plots at the indicated instants for the 2D decaying turbulence problem

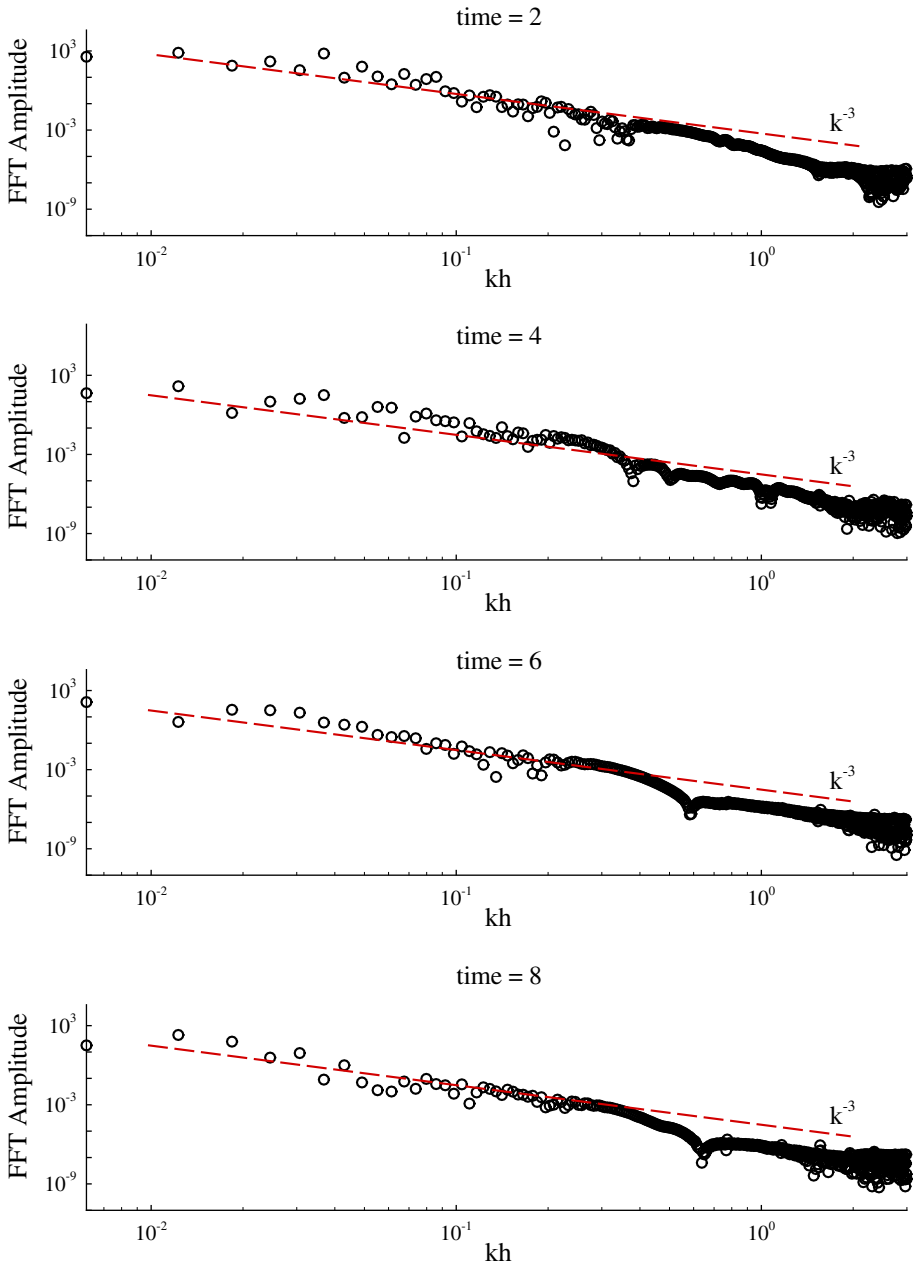

Fig. 18 Variation of 1D energy spectrum at the indicated instants for the 2D decaying turbulence problem

flow field and half width of the container as a characteristic length scale. High resolution numerical simulations of 2D decaying turbulence are previously reported in [37,38,40]. We have analyzed our numerical results with the flow development stages given in these previous works.

Results in [37] suggested that there are two specific aspects of the 2D decaying turbulence flow dynamics. The first aspect is related to the formation of small scale structures in the form of vorticity gradient sheets and second characteristic aspect is related to the emergence of coherent vorticity structures. Three important stages of development of 2D decaying turbulence were shown in [37]. In the initial stage, rapid self organization is observed in which similar-sign vortices merge with each other and form a medium sized dipoles. This is also accompanied by steepening vorticity gradients due to strong interaction between the individual vortices and the formation of boundary layer on the container walls. Intense interaction between the vortices close to wall and the boundary layer either causes ejection of thin vorticity filaments in the interior domain or results in formation of vorticity blob. These newly emerged secondary vortex structures form the dipolar structure with the primary vortex which is responsible for its creation. In the second stage, there is a strong interaction between vortices and wall boundary layer and this stage shows formation of the eddies whose sizes are comparable to that of the size of container. In the third stage, decaying nature of the flow causes formation of the large monopolar structure close to the center of the domain.

We have shown different stages of flow evolution in Fig. 17. One can observe formation of boundary layer at the early time $t = 2$ frame on the sides of the container. As flow evolves, like sign vortices merge with each other and form medium sized dipoles as shown in the frames $t = 5$ and $t = 10$. Ejection of thin vorticity strips and vorticity blobs from the boundary layer are visible at $t = 10$. At $t = 50$, eddies with size comparable to container size are formed. We have further obtained one dimensional energy spectrum by considering velocity distribution on the line $y = -0.22$ as shown in Fig. 18. At different instants, figure shows k^{-3} spectrum which is an indication of 2D turbulence. Thus the developed high accuracy schemes are very useful in the computations of fluid flow involving large bandwidth of spatio-temporal scales.

7 Summary and Conclusions

In this manuscript, we have proposed two new CCD schemes to obtain better numerical properties as compared to the CCD schemes in [1,20]. The first scheme A has an upwind stencil which is derived to get better numerical properties as compared to the upwind CCD scheme in [1]. The second scheme B has a central stencil and is derived to get better numerical properties as compared to the central CCD scheme in [20]. This scheme has slightly improved resolution as compared to the CCD scheme in [20] as shown in Fig. 1a. It has neutrally stable region along the complete wavenumber range for small CFL values but it also has a significant q-wave region as shown in Figs. 4d and 5d. When the steep gradients are present in the solution, the computations performed with scheme B show q-waves as displayed in Figs. 6d, 7d and 9d. For a lid driven cavity flow at $Re = 10^4$, computations using the CCD scheme B show presence of higher wavenumber oscillations near the top right corner and these calculations are susceptible to the aliasing error as pointed out in Fig. 13.

However, the proposed scheme A has the highest spectral resolution as compared to all the CCD methods. Additionally, it has an added numerical diffusion which is restricted to only high wavenumber region. As proposed in [11,27,28], one can use such upwind numerical schemes to control aliasing error present for high wavenumber components and perform large eddy simulations. The proposed scheme A is very much suitable for large eddy simulation calculations from this point of view. This scheme has higher neutrally stable region as compared to the upwind CCD scheme of [1] and has the best DRP properties, as shown in Figs. 4c and 5c, respectively. Additionally, this scheme has the least q-wave region corresponding to the high wavenumber region which is highly attenuated with an

added numerical diffusion. This also helps to avoid use of an extra filtering process in order to remove q-waves from the solution suggested in [30]. Computations with the scheme A do not show dominant q-waves as observed from Figs. 6c, 7c and 9c. Additionally, the upwind nature of scheme A helps to control aliasing error as seen from the lid driven cavity results for $Re = 10^4$ in Fig. 13. Thus, use of the upwind CCD scheme A is very beneficial for obtaining a highly space-time accurate solution as observed from the results for 2D decaying turbulence problem in Figs. 17 and 18.

Acknowledgments This work was supported by the National Science Council of the Republic of China under Grant 101R891002. We are thankful to Prof. Tapan K. Sengupta for his valuable suggestions in the preparation of this manuscript.

Appendix

In this section, we have provided the steps while developing an upwind combined compact difference scheme. The first and the second derivative terms ($\frac{\partial u}{\partial x}$ and $\frac{\partial^2 u}{\partial x^2}$) are approximated as

$$a_1 \frac{\partial u}{\partial x}|_{i-1} + \frac{\partial u}{\partial x}|_i + a_3 \frac{\partial u}{\partial x}|_{i+1} = \frac{1}{h}(c_1 u_{i-2} + c_2 u_{i-1} + c_3 u_i) - h\left(b_1 \frac{\partial^2 u}{\partial x^2}|_{i-1} + b_2 \frac{\partial^2 u}{\partial x^2}|_i + b_3 \frac{\partial^2 u}{\partial x^2}|_{i+1}\right), \tag{30}$$

$$-\frac{1}{8}\frac{\partial^2 u}{\partial x^2}|_{i-1} + \frac{\partial^2 u}{\partial x^2}|_i - \frac{1}{8}\frac{\partial^2 u}{\partial x^2}|_{i+1} = \frac{3}{h^2}(u_{i-1} - 2u_i + u_{i+1}) - \frac{9}{8h}\left(-\frac{\partial u}{\partial x}|_{i-1} + \frac{\partial u}{\partial x}|_{i+1}\right). \tag{31}$$

Here, we have used a central stencil to approximate the second-order derivative term. Taylor series expansion has been used to obtain the coefficients shown in (31), which results in a sixth-order accurate stencil based on the leading truncation error term. Coefficients in Eq. (30) are obtained by applying the Taylor series expansion for the terms u_{i-1}, u_{i+1}, $\frac{\partial u}{\partial x}|_{i-1}$, $\frac{\partial u}{\partial x}|_i$, $\frac{\partial u}{\partial x}|_{i+1}$, $\frac{\partial^2 u}{\partial x^2}|_{i-1}$, $\frac{\partial^2 u}{\partial x^2}|_i$ and $\frac{\partial^2 u}{\partial x^2}|_{i+1}$ with respect to u_i.

In Eq. (30), there are in total eight unknown coefficients. Elimination of the leading truncation error terms gives the following set of seven algebraic equations.

$$c_1 + c_2 + c_3 = 0, \tag{32}$$

$$-2c_1 - c_2 - a_1 - a_3 = 1, \tag{33}$$

$$4c_1 + c_2 + 2a_1 - 2a_3 - 2b_1 - 2b_2 - 2b_3 = 0, \tag{34}$$

$$8c_1 + c_2 + 3a_1 + 3a_3 - 6b_1 + 6b_3 = 0, \tag{35}$$

$$16c_1 + c_2 + 4a_1 - 4a_3 - 12b_1 - 12b_3 = 0, \tag{36}$$

$$32c_1 + c_2 + 5a_1 + 5a_3 - 20b_1 + 20b_3 = 0, \tag{37}$$

$$64c_1 + c_2 + 6a_1 - 6a_3 - 30b_1 - 30b_3 = 0. \tag{38}$$

Derivation of one more algebraic equation is needed to determine all the eight coefficients in Eq. (30) uniquely for $\frac{\partial u}{\partial x}|_i$. The first-order derivative term in Eq. (30) can be better approximated if the dispersive nature of the term $\frac{\partial u}{\partial x}$ is well retained [1].

The expressions of the actual wavenumber for Eqs. (30) and (31) can be derived as

$$\mathbf{i}\alpha h\,(a_1 e^{-\mathbf{i}\alpha h} + 1 + a_3 e^{\mathbf{i}\alpha h}) \simeq \left(c_1 e^{-2\mathbf{i}\alpha h} + c_2 e^{-\mathbf{i}\alpha h} + c_3\right) - (\mathbf{i}\alpha h)^2 \left(b_1 e^{-\mathbf{i}\alpha h} + b_2 + b_3 e^{\mathbf{i}\alpha h}\right), \tag{39}$$

$$(\mathbf{i}\alpha h)^2 \left(-\frac{1}{8} e^{-\mathbf{i}\alpha h} + 1 - \frac{1}{8} e^{\mathbf{i}\alpha h}\right) \simeq (3e^{-\mathbf{i}\alpha h} - 6 + 3e^{\mathbf{i}\alpha h}) - \mathbf{i}\alpha h \left(-\frac{9}{8} e^{-\mathbf{i}\alpha h} + \frac{9}{8} e^{\mathbf{i}\alpha h}\right). \tag{40}$$

While approximating the first-order derivative term, dispersion error is minimized if the exact and the numerical wavenumbers are matched excellently over a complete wavenumber range. This amounts to equating the effective wavenumbers $\alpha^{'}$ and $\alpha^{''}$ to those shown in the right-hand sides of Eqs. (41) and (42) [1]. Thus, we obtained following two equations

$$\mathbf{i}\alpha^{'} h \left(a_1 e^{-\mathbf{i}\alpha h} + 1 + a_3 e^{\mathbf{i}\alpha h}\right) = \left(c_1 e^{-2\mathbf{i}\alpha h} + c_2 e^{-\mathbf{i}\alpha h} + c_3\right) - \left(\mathbf{i}\alpha^{''} h\right)^2 \left(b_1 e^{-\mathbf{i}\alpha h} + b_2 + b_3 e^{\mathbf{i}\alpha h}\right), \tag{41}$$

$$(\mathbf{i}\alpha^{''} h)^2 \left(-\frac{1}{8} e^{-\mathbf{i}\alpha h} + 1 - \frac{1}{8} e^{\mathbf{i}\alpha h}\right) = (3e^{-\mathbf{i}\alpha h} - 6 + 3e^{\mathbf{i}\alpha h}) - \mathbf{i}\alpha^{'} h \left(-\frac{9}{8} e^{-\mathbf{i}\alpha h} + \frac{9}{8} e^{\mathbf{i}\alpha h}\right). \tag{42}$$

Equations (41) and (42) are solved to get the expression for $\alpha' h$ which has been used subsequently to minimize the dispersion error. This expression for $\alpha' h$, which is in general complex with the real and imaginary parts of the numerical modified wavenumber $\alpha' h$, provides information regarding the dispersion error (phase error) and the dissipation error (amplitude error), respectively. For getting better dispersive accuracy of α', the value of αh should be closer to $\Re[\alpha' h]$, where $\Re[\alpha' h]$ denotes the real part of $\alpha' h$. Thus the error function $E(\alpha)$ as defined below should be very small. It has been evaluated over the integration range given below as

$$E(\alpha) = \int_0^{\frac{7\pi}{8}} \left[\left(\alpha\, h - \Re[\alpha'\, h]\right)\right]^2 d(\alpha h). \tag{43}$$

To make the error function defined in $0 \le \alpha h \le \frac{7\pi}{8}$ to be positive and minimal, the extreme condition $\frac{\partial E}{\partial c_3} = 0$ is enforced to minimize the numerical wavenumber error. This constraint equation has been used together with previously derived seven algebraic equations to obtain all the eight unknowns. The resulting eight introduced unknown coefficients can be uniquely determined as

$$a_1 = 0.888251792581,\ a_3 = 0.049229651564, b_1 = 0.150072398996,$$
$$b_2 = -0.250712794122,\ b_3 = -0.012416467490,\ c_1 = 0.016661718438,$$
$$c_2 = -1.970804881023\, and\, c_3 = 1.954143162584.$$

For $u < 0$, the proposed three-point stencil non-centered combined compact difference scheme can be similarly derived below for the approximation of the derivative term $\frac{\partial u}{\partial x}$

$$0.049229651564\frac{\partial\phi}{\partial x}|_{i-1}+\frac{\partial\phi}{\partial x}|_{i}+0.888251792581\frac{\partial\phi}{\partial x}|_{i+1}$$
$$+\,h\Big(0.012416467490\frac{\partial^2\phi}{\partial x^2}|_{i-1}+0.250712794122\frac{\partial^2\phi}{\partial x^2}|_{i}-0.150072398996\frac{\partial^2\phi}{\partial x^2}|_{i+1}\Big)$$
$$=\frac{1}{h}\left(-1.954143162584\phi_i+1.970804881023\phi_{i+1}-0.016661718438\phi_{i+2}\right). \qquad (44)$$

One should pay a careful attention to the following important points. Significant improvements in spectral resolution as shown in Fig. 1e and the DRP region shown in Fig. 5 are possible using a small stencil because we have derived the scheme for first and second derivatives in a coupled fashion. The expression for $\alpha^{'}h$ is derived by considering Eqs. (41) and (42) together. Figure 1f shows that efficiency in the evaluation of the second derivative is very close to the exact value. Thus, while designing CCD schemes, use of one optimization equation given by $\frac{\partial E}{\partial c_3}=0$ is justified.

References

1. Chiu, P.H., Sheu, T.W.H.: On the development of a dispersion-relation-preserving dual-compact upwind scheme for convection-diffusion equation. J. Comput. Phys. **228**, 3640–3655 (2009)
2. Sengupta, T.K., Dipankar, A., Sagaut, P.: Error dynamics: beyond von Neumann analysis. J. Comput. Phys. **226**, 1211–1218 (2007)
3. Tam, C.K.W., Webb, J.C.: Dispersion-relation-preserving finite difference schemes for computational acoustics. J. Comput. Phys. **107**, 262–281 (1993)
4. Lele, S.K.: Compact finite difference schemes with spectral-like resolution. J. Comput. Phys. **103**, 16–42 (1992)
5. Sengupta, T.K., Ganeriwal, G., De, S.: Analysis of central and upwind compact schemes. J. Comput. Phys. **192**, 677–694 (2003)
6. Sengupta, T.K., Sircar, S.K., Dipankar, A.: High accuracy schemes for DNS and acoustics. J. Sci. Comput. **26**, 151–193 (2006)
7. Weinan, E., Liu, J.G.: Essentially compact schemes for unsteady viscous incompressible flows. J. Comput. Phys. **126**, 122–138 (1996)
8. Meitz, H.L., Fasel, H.F.: A compact-difference scheme for the Navier–Stokes equations in vorticity-velocity formulation. J. Comput. Phys. **157**, 371–403 (2000)
9. Lee, C., Seo, Y.: A new compact spectral scheme for turbulence simulations. J. Comput. Phys. **183**, 438–469 (2002)
10. Nagarajan, S., Lele, S.K.: A robust high order compact method for large eddy simulation. J. Comput. Phys. **191**, 392–419 (2003)
11. Park, N., Yoo, J.Y., Choi, H.: Discretization errors in large eddy simulation: on the suitability of centered and upwind biased compact difference schemes. J. Comput. Phys. **198**, 580–616 (2004)
12. Zhong, X.: High-order finite-difference schemes for numerical simulation of hypersonic boundary-layer transition. J. Comput. Phys. **144**, 662–709 (1998)
13. Sengupta, T.K., Rajpoot, M.K., Bhumkar, Y.G.: Space-time discretizing optimal DRP schemes for flow and wave propagation problems. Comput. Fluids **47**, 144–154 (2011)
14. Ekaterinaris, J.A.: Implicit, high-resolution compact schemes for gas dynamics and aeroacoustics. J. Comput. Phys. **156**, 272–299 (1999)
15. Shang, J.S.: High-order compact-difference schemes for time-dependent maxwell equations. J. Comput. Phys. **153**, 312–333 (1999)
16. Zhou, Q., Yao, Z., He, F., Shen, M.Y.: A new family of high-order compact upwind difference schemes with good spectral resolution. J. Comput. Phys. **227**, 1306–1339 (2007)
17. Mahesh, K.: A family of high order finite difference schemes with good spectral resolution. J. Comput. Phys. **145**, 332–358 (1998)
18. Dipankar, A., Sengupta, T.K.: Symmetrized compact scheme for receptivity study of 2D transitional channel flow. J. Comput. Phys. **215**, 245–273 (2006)
19. Sengupta, T.K.: High Accuracy Computing Methods: Fluid Flows and Wave Phenomena. Cambridge University Press, Cambridge, MA (2013)

20. Chu, P.C., Fan, C.: A three-point combined compact difference scheme. J. Comput. Phys. **140**, 370–399 (1998)
21. Sengupta, T.K., Lakshmanan, V., Vijay, V.V.S.N.: A new combined stable and dispersion relation preserving compact scheme for non-periodic problems. J. Comput. Phys. **228**, 3048–3071 (2009)
22. Sengupta, T.K., Vijay, V.V.S.N., Bhaumik, S.: Further improvement and analysis of CCD scheme: dissipation discretization and de-aliasing properties. J. Comput. Phys. **228**, 6150–6168 (2009)
23. Arakawa, A.: Computational design of long term numerical integration of the equations of fluid motion: two-dimensional incompressible flow. J. Comput. Phys. **1**, 119–143 (1966)
24. Kennedy, C.A., Gruber, A.: Reduced aliasing formulations of the convective terms within the Navier–Stokes equations for a compressible fluid. J. Comput. Phys. **227**, 1676–1700 (2008)
25. Kirby, R.M., Karniadakis, G.E.: De-aliasing on non-uniform grids: algorithms and application. J. Comput. Phys. **191**, 249–264 (2003)
26. Sengupta, T.K., Bhaumik, S., Bhumkar, Y.G.: Direct numerical simulation of two-dimensional wall-bounded turbulent flows from receptivity stage. Phys. Rev. E. **85**, 026308 (2012)
27. Sengupta, T.K., Nair, M.T.: Upwind schemes and large eddy simulation. Int. J. Numer. Methods Fluids **31**, 879–889 (1999)
28. Lesieur, M., Metais, O.: New trends in large eddy simulation of turbulence. Annu. Rev. Fluid Mech. **28**, 45–82 (1996)
29. Sengupta, T.K., Dipankar, A.: A comparative study of time advancement methods for solving Navier–Stokes equations. J. Sci. Comput. **21**, 225–250 (2004)
30. Sengupta, T.K., Bhumkar, Y.G., Rajpoot, M., Suman, V.K., Saurabh, S.: Spurious waves in discrete computation of wave phenomena and flow problems. Appl. Math. Comput. **218**, 9035–9065 (2012)
31. Sheu, T.W.H., Chiu, P.H.: A divergence-free-condition compensated method for incompressible Navier–Stokes equations. Comput. Methods Appl. Mech. Eng. **196**, 4479–4494 (2007)
32. Green, S.I.: Fluid Vortices: Fluid Mechanics and Its Applications. Springer, Berlin (1995)
33. Ghia, U., Ghia, K.N., Shin, C.T.: High-Re solutions for incompressible flow using the Navier–Stokes equations and a multigrid method. J. Comput. Phys. **48**, 387–411 (1982)
34. Botella, O., Peyret, R.: Benchmark spectral results on the lid-driven cavity flow. Comput. Fluids **27**, 421–433 (1998)
35. Bruneau, C.-H., Saad, M.: The 2D lid-driven cavity problem revisited. Comput. Fluids **35**, 326–348 (2006)
36. Peng, Y.F., Shiau, Y.H., Hwang, R.R.: Transition in a 2D lid driven cavity flow. Comput. Fluids **32**, 337–352 (2003)
37. Clercx, H.J.H., Maassen, S.R., van Heijst, G.J.F.: Decaying two-dimensional turbulence in square containers with no-slip or stress-free boundaries. Phys. Fluids **11**, 611–626 (1999)
38. Clercx, H.J.H., van Heijst, G.J.F.: Energy spectra for decaying 2D turbulence in a bounded domain. Phys. Rev. Lett. **85**, 306–309 (2000)
39. Sengupta, T.K., Singh, H., Bhaumik, S., Chowdhury, R.R.: Diffusion in inhomogeneous flows: unique equilibrium state in an internal flow. Comput. Fluids **88**, 440–451 (2013)
40. Braccoa, A., McWilliams, J.C., Murante, G., Provenzale, A., Weiss, J.B.: Revisiting freely decaying two-dimensional turbulence at millennial resolution. Phys. Fluids **12**, 2931–2941 (2000)
41. Lo, D.C., Murugesan, K., Young, D.L.: Numerical solution of three-dimensional velocity–vorticity incompressible Navier–Stokes equations by finite difference method. Int. J. Numer. Methods Fluids **47**, 1469–1487 (2005)
42. Ding, H., Shu, C., Yeo, K.S., Xu, D.: Numerical computation of three-dimensional incompressible viscous flows in the primitive variable form by local multiquadric differential quadrature method. Comput. Methods Appl. Mech. Eng. **195**, 516–533 (2006)